Climate Dynamics
https://doi.org/10.1007/s00382-022-06164-w

On the weakening of northward propagation of intraseasonal oscillations during positive Indian Ocean Dipole events

Aditya Kottapalli[1] · **P. N. Vinayachandran**[1]

Received: 31 May 2021 / Accepted: 21 January 2022

Abstract
The northward propagation of intraseasonal oscillations (ISO) is one of the major modes of variability in the tropics during boreal summers, associated with active and break spells of monsoon rainfall over the Indian region. These northward propagations modulate the Indian summer monsoon rainfall. The northward march starts close to the equator over warm waters of the Indian Ocean and continues till the foothills of the Himalayas. In this study, we investigate the influence of Indian Ocean Dipole (IOD) on northward propagations. We show that northward propagations tend to be weaker during positive Indian Ocean Dipole (pIOD) events. The "moisture mode" framework is used to understand the processes responsible for the weakening of northward propagations during pIOD years. Our analyses show that moistening caused by the horizontal advection is the major contributor for the northward propagations during negative IOD (nIOD) years, and its amplitude is much smaller during pIOD years. Further analyses revealed that the reduction in the advection of the background entropy/moisture by zonal wind perturbations during pIOD is primarily responsible for the reduction in the horizontal advection. The mean structure of entropy between 925 and 500 hpa levels remained similar over most of the Asian monsoon region across the contrasting IOD years, and the reason for weaker northward propagations can be attributed to the weaker zonal wind perturbations at intraseasonal timescales. These weaker zonal wind perturbations during ISO events in pIOD years results from weak Rossby Vortex lobes. The weakening of Rossby wave response owing to cooler than average sea surface temperatures in the South-East Equatorial Indian Ocean and warmer than average West Equatorial Indian Ocean is proposed to be the possible reason for the weakening of northward propagations during pIOD years.

Keywords IOD · DMI · Moisture mode · Moist entropy · SST

1 Introduction

The northward propagations of cloud bands from the equator over to the monsoon regions of southeast Asia are associated with the active and break spells of the Indian monsoon (Yasunari 1979; Sikka and Gadgil 1980; Krishnamurti and Subramanyam 1982). Using daily satellite mosaic pictures, Yasunari (1979) found two dominant periodicities in cloudiness fluctuations, of 40 days and 15 days, out of which the 40-day fluctuations showed marked northward movement of cloudiness from equatorial zone to mid-latitudes. This northward movement was most apparent in the Indian Ocean sector. Sikka and Gadgil (1980), using satellite images along with 700 mb trough data, found that there were two favourable locations for maximum cloud zone (MCZ) during the summer monsoon, one over the monsoon zone to the north of 15° N latitude and the other over the equatorial region (0° N–10° N). They observed that the MCZ over the monsoon zone could not survive for a long time without being re-established by MCZ over the ocean by the northward propagation. Krishnamurti and Subramanyam (1982) analyzed wind fields at 850 hpa during the summer monsoon experiment (MONEX) and confirmed the existence of a peak in 30–50 days' time range. They also illustrated the propagation of trains of troughs and ridges from the equator to the Himalayas. They found that the meridional scale of propagation was around 3000 km, and the speed was about 0.75°–1°/day.

Considerable efforts have been made in the last 5 decades to understand the mechanisms responsible for the northward

✉ Aditya Kottapalli
adityak1@iisc.ac.in

[1] Centre for Atmospheric and Oceanic Sciences and Divecha Centre for Climate Change, Indian Institute of Science, Bengaluru, India

Published online: 15 February 2022

propagations. Webster (1983) suggested that the hydrological feedback leads to cooling of land beneath the Tropical Convergent Zone (TCZ), createing a poleward gradient of sensible heat flux in the boundary layer, leading to the poleward propagations. But this mechanism could not explain the propagations over the ocean. Gadgil and Srinivasan (1990) showed that adding thermal inertia to the land and realistic sea surface temperatures (SST) to Webster's model could help in a more realistic simulation of poleward propagations. They further understood that TCZ propagates north from the genesis point because of excess heating to the north of TCZ. This excess heating causes the intensification of ascent in the region to the north of the ascent axis, resulting in the northward propagation of TCZ. Nevertheless, this model could not simulate the active phase of monsoon at the end of each propagation, rather the TCZ over the continent disappeared abruptly, and the following propagation commenced. Nanjundiah et al. (1992) used a zonally symmetric model which incorporated space–time variation of surface pressure. This model simulated the poleward propagations more realistically; it also simulated the TCZ persisting over the continental trough for 20 days. The emanation of Equatorial Rossby waves from Equatorial convection was proposed to be responsible for northward propagations by some studies (e.g., Wang and Xie 1997; Lawrence and Webster 2002). Jiang et al. (2004) proposed that barotropic vorticity develops in the atmosphere ahead of the convection centre in the presence of vertical shear. This barotropic vorticity induces convergence in the boundary layer through Ekman pumping, leading to a northward shift of convective heating.

Along with the convection, the SST also show intraseasonal oscillation signals (Krishnamurti et al. 1988; Sengupta and Ravichandran 2001; Sengupta et al. 2001; Bhat et al. 2001). Though SST signals could result from atmospheric forcing, they help enhance convergence to the north of the convection centre, guiding the northward propagations. Through their model experiments, Fu et al. (2003) showed that atmosphere—only models could not simulate the northward propagations even when forced with daily SSTs from the coupled run, suggesting the role of high-frequency air–sea interactions in northward propagations.

The SSTs over the equatorial Indian Ocean are modulated by Indian Ocean Dipole (IOD) (Saji et al. 1999; Webster et al. 1999). IOD is a coupled Ocean atmospheric phenomenon that is manifested by the anomalous warming (cooling) of the Eastern Equatorial Indian Ocean (EEIO) and simultaneous cooling (warming) of the Western Equatorial Indian Ocean (WEIO). In its positive phase, WEIO is anomalously warmer than EEIO and vice versa. Since northward propagations start close to the equator, it is interesting to ask, "How would IOD affect the northward propagations?" Though the IOD peaks after the monsoon, the SST anomalies in the equatorial Indian ocean shows the signal during the monsoon time itself. Ashok et al. (2001) found that IOD plays a vital role in modulating the Indian summer monsoon rainfall (ISMR) and influences the ISMR—ElNino and the Southern Oscillation (ENSO) relation. Gadgil et al. (2004) noticed that larger anomalies in the ISMR are linked with the Equatorial Indian Ocean oscillation (EQUINOO), which can be considered the atmospheric component of the coupled IOD. The impact of IOD on global climate was explored by Saji and Yamagata (2003). They noted the impact of IOD on several regions even remote to the Indian Ocean, with strong correlations over Europe, northeast Asia, North and South America and South Africa co-occurring with IOD events. Vinayachandran et al. (2009) reviewed the relationship between IOD and the regional climate over the Indian Ocean and surrounding landmass. They documented that IOD events affect the rainfall over the maritime continent, Australia, the Indian subcontinent, and East Africa. While the maritime continent and Australia experience a deficit in rainfall during positive IOD (pIOD) years, East Africa and India experience excess rainfall.

Ajayamohan et al. (2008) investigated the role of IOD in modulating the northward propagations and found out the coherent (incoherent) nature of propagations during negative (positive) IOD years. They also found that the dynamical features suggested by Jiang et al. (2004) for the northward propagation were absent during pIOD years leading to incoherent northward propagations. According to them, the mean structure of specific humidity in South-East Equatorial Indian Ocean (SEIO) undergoes radical changes during contrasting IOD years. Also, the meridional gradient of specific humidity is enhanced (suppressed) during nIOD (pIOD) years leading to coherent (incoherent) propagations. However, observations show that the meridional gradient of specific humidity between 5° S and the equator was higher during pIOD years. Thus, it is not clear why northward propagations are incoherent during pIOD years. Also, the processes responsible for these incoherent propagations during pIOD years remain unexplored. Thus, this study's objective is to understand in detail "How would the northward propagations gets modulated by the IOD?" and "What are the processes responsible for this modulation?"

To answer these questions, we use the "moisture mode" framework, which has been recently applied extensively for understanding the eastward propagations of Madden Julian Oscillations (MJO) (e.g., Maloney 2009; Sobel and Maloney 2012, 2013; Adames and Wallace 2015; Adames and Kim 2016). It was revealed from the past studies that the horizontal advection of moist static energy (MSE) is responsible for the eastward propagation of MJO related convection (e.g., Maloney 2009; Jiang 2017). In boreal winters, the maxima in the mean specific humidity lie between 140° E and 150° E longitudes close to the equator with the strong poleward and westward gradients, which helps in the eastward propagation

of MJO (Adames et al. 2016). Jiang et al. (2018) extended this moisture mode to northward propagations. They found that the boreal summer's mean moisture structure is responsible for northward propagations like in the boreal winter. During boreal summers, the maximum in specific humidity is displaced to around 20° N over the Indo-China region, leading to northward propagation. Our analysis using the "moisture mode" framework to understand the differences in the northward propagations during pIOD and nIOD years revealed that the mean structure of the specific humidity/entropy does not change much across contrasting IOD years. On the other hand, we find that the weakening of the northward propagations during pIOD years can be attributed to the weak perturbations of zonal wind at intraseasonal time scales.

Our study in this paper is organized as follows: Sect. 2 describes the data used in our analysis. Section 3 discusses the methods used and some discussion on differences between pIOD and nIOD years. Section 3.1 deals with methods used to identify pIOD and nIOD years. In Sect. 3.2, we discuss the differences in the mean structure between contrasting IOD years. Section 3.3 is dedicated to the methods used to visualize the northward propagations and understanding the differences in the northward propagations across contrasting IOD years. Section 4 exclusively deals with moist entropy and its budget. Section 5 proposes a possible mechanism that helps understand the weakening of northward propagation during pIOD years. Section 6 summarizes our analysis.

2 Data

The interpolated outgoing longwave radiation (OLR) from the National Ocean and Atmospheric Administration (NOAA) (Liebmann and Smith 1996) was used as a proxy for rainfall (Gadgil et al. 2002). The air temperature, relative humidity, u-wind, v-wind and vertical pressure velocity were obtained from National Centres for Environmental Predictions (NCEP) reanalysis—2 data provided by the NOAA/OAR/ESRL PSL, Boulder, Colorado, USA, from their Web site at https://psl.noaa.gov/data/gridded/data.ncep.reanalysis2.html was used. The OLR and reanalysis—2 data have a horizontal resolution of 2.5°×2.5°, and there are 17 levels vertically from 1000 hpa level to 10 hpa level. High-resolution 0.25°×0.25° SST anomaly data OISST (Huang 2020) from NOAA was used for calculating the Dipole Mode Index (DMI) to categorize the IOD years based on the June–July–August–September (JJAS) mean DMI index (Saji et al. 1999). The surface heat fluxes were taken from OAFlux (Yu et al. 2008) with the spatial resolution of 1°×1°. The OAFlux data was only available over oceans but, the residues from this error are small enough to be neglected (Jiang et al. 2018). All the data used in the analysis has a temporal resolution of 1 day. High-resolution 0.25°×0.25° ERA 5, hourly radiation data (Hersbach et al. 2018) was used to calculate radiative fluxes, the data has been averaged to get the daily mean. All the data (except SST) were re gridded to 2.5°×2.5° using bilinear interpolation technique to match the OLR/reanalysis data.

3 Methods and discussion

3.1 Identifying pIOD and nIOD years

We start with differentiating the monsoon period (JJAS) into contrasting IOD (positive/negative) years. Following Saji et al. (1999), the strength of an IOD event is determined using the Dipole Mode Index (DMI), defined as the difference in the area-averaged SST anomalies between the WEIO (50° E–70° E, 10° S–10° N) and EEIO (90° E–110° E, 10° S–0) normalized by the standard deviation (SD). Since we are interested in the summer monsoon, the JJAS mean DMI is used for associating a particular monsoon period into positive IOD, negative IOD or neutral categories. The same JJAS DMI criteria were used by Ajayamohan et al. (2008) to identify pIOD and nIOD events. Also, the SSTs in the EEIO are climatologically higher than in the WEIO, and a positive SST anomaly in EEIO means more convection over the EEIO than the WEIO despite positive anomaly there, which we are not interested in this study. Thus, we impose the anomalous cooling criteria over the EEIO and the JJAS DMI criteria for associating a monsoon period into pIOD. The nIOD association is entirely based on the DMI.

The criteria we followed is:

(a) If JJAS $DMI > 0.5 \times SD$ and the EEIO show anomalous cooling, we would select that as a positive IOD year.
(b) If JJAS $DMI < -0.5 \times SD$, the year is marked as a negative IOD year.

The analysis is based on 35 years of SST data from 1985 to 2019. Figure 1 shows the JJAS mean DMI index for the data analyzed. Among the years shown in Fig. 1, those that did not satisfy the eastern box cooling criteria are 2007, 2015, and 2017 which were excluded from our analysis despite having a positive DMI. The years considered as pIOD and nIOD are tabulated in Table 1.

3.2 Difference in the mean structure across contrasting IOD years

First, we examine the difference in the mean SST, OLR, and winds between pIOD and nIOD years. Figure 2 shows the mean JJAS SST anomalies for pIOD, nIOD and the difference between pIOD and nIOD years, along with the regions mentioned earlier for calculating the DMI. The dipole in

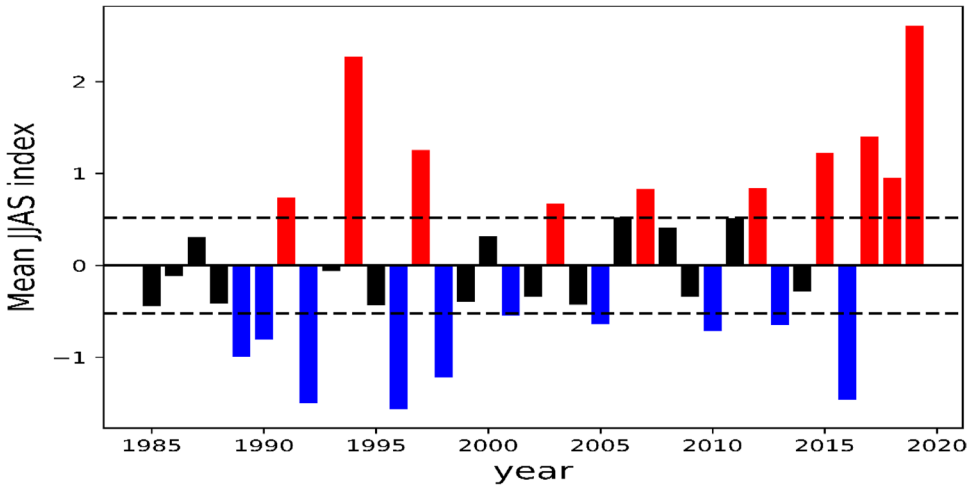

Fig. 1 The mean JJAS DMI from 1985 to 2019, years in which JJAS DMI crossed the + 0.5 × SD values are marked in red, those years when the JJAS DMI values were less than − 0.5 × SD are marked in blue, and the rest in black. The dashed lines show + − 0.5 SD values

Table 1 pIOD and nIOD years

pIOD	nIOD
1991, 1994, 1997, 2003, 2012, 2018, 2019	1989, 1990, 1992, 1996, 1998, 2001, 2005, 2010, 2013, 2016

the SST anomaly is evident. Interestingly, the pIOD pattern (Fig. 2a) is marked by warm SST anomalies over a large region around and south of India. During nIOD years,

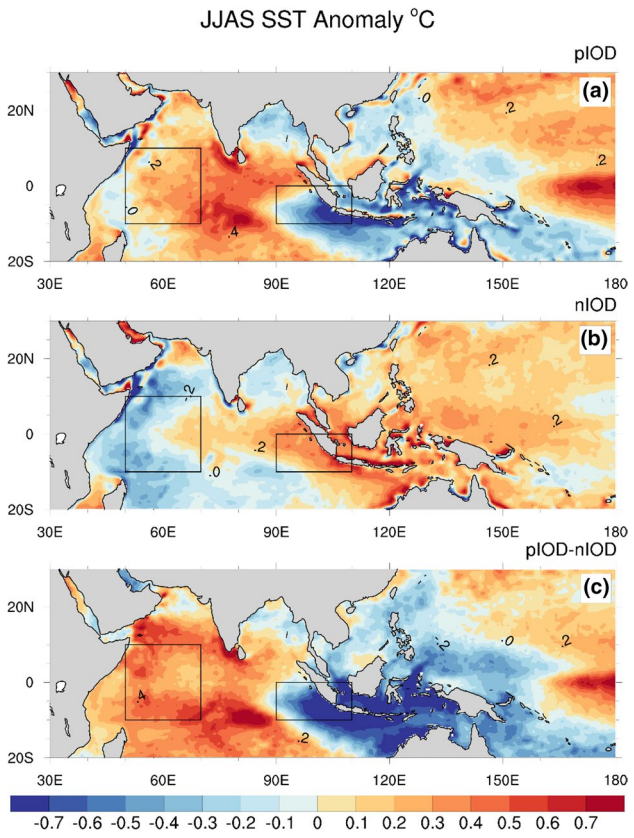

Fig. 2 The mean JJAS SST (°C) anomalies for **a** pIOD, **b** nIOD and **c** difference between pIOD and nIOD years, the black boxes show the western and eastern boxes used for calculating the DMI

the warm anomalies that are highest in the EEIO extend as an equatorial tongue up to about 60 E (Fig. 2b). The SST anomaly patterns simply do not reverse from pIOD to nIOD. Figure 3 shows the difference in the mean OLR anomalies along with mean 850 hpa winds; comparing with Figure 2, the regions of higher SST are the regions with negative OLR anomalies and vice versa, which signifies the role of SST in generating/enhancing the convection over the Equatorial Oceans. Though the wind pattern looks similar between pIOD and nIOD years at first glance, the difference between the two is evident (Fig. 3c) where the anomalous south-easterly winds from EEIO to central Equatorial Indian Ocean during pIOD years can be seen.

3.3 Differences in northward propagation across contrasting IOD years

To understand the differences in northward propagations across contrasting IOD years, we use daily OLR anomalies obtained by removing the daily climatology from the time series at each grid point. The OLR anomalies are then filtered using a 25–80 days recursive Butterworth bandpass filter (hereafter referred to as ISO filtered), after removing the mean from the time series. The Butterworth bandpass filter was extensively used in past studies for extracting ISO signals (e.g., Krishnamurti and Subramanyam 1982; Goswami et al. 1998; Misra et al. 2012, 2018). The evolution composites of ISO filtered OLR anomalies are then constructed from individual cycles for nIOD and pIOD years (Table 1). The northward propagations are more apparent over the Indian Ocean sector (Yasunari 1979; Jiang et al. 2018), and the strength of ISO convection is maximum between latitudes

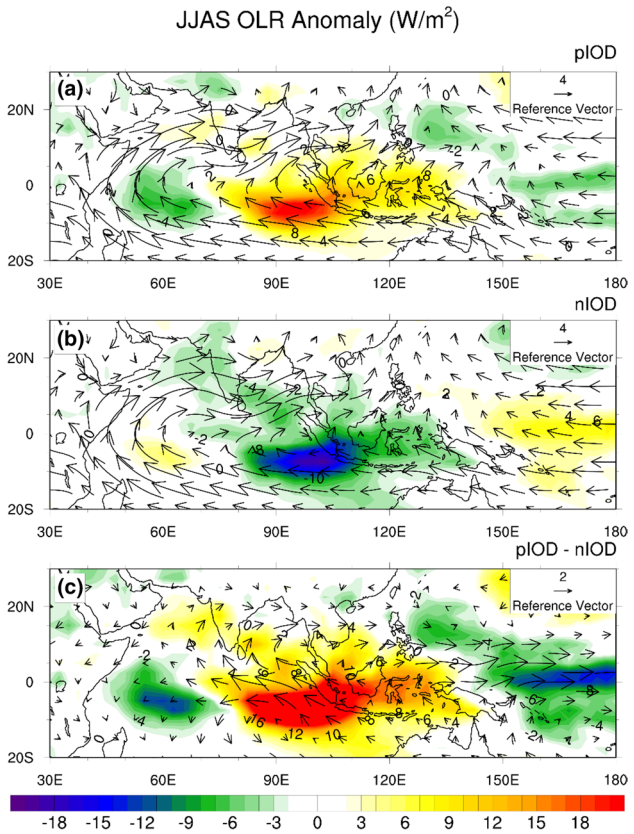

Fig. 3 The mean JJAS OLR (W/m^2) anomalies and 850 hpa wind vectors (m/s) for **a** pIOD, **b** nIOD and **c** difference between pIOD and nIOD years. The reference vectors are shown to the top right of each panel

5° N and 10° N (e.g., Jiang et al. 2004). Thus, we construct composites in such a way that on lag 0 days, the minima of ISO filtered OLR (maxima of ISO convection) falls over the region 2.5° N–7.5° N and 70° E–95° E (centred at 5° N).

Figure 4 shows the evolution composite of ISO filtered OLR anomaly for nIOD years. The convection initiates at lag 12 days (Fig. 4b) close to 60° E, along the equator. The convection then strengthens moving eastward, and, by lag 6 days, strong convection can be seen over central and EEIO (between 80° E and 90° E longitudes) along the equator (Fig. 4d). The convection further intensifies, and by lag 3 days, the convection centre reaches 90° E (Fig. 4e), subsequently propagating northward. The convection centre reaches peninsular India by lead 6 days (Fig. 4h), and central India by lead 9 days (Fig. 4i). A hint of southward propagation (Fig. 4f–h) off Sumatra is also seen, as pointed out in Lawrence and Webster (2002).

Figure 5 shows the evolution composite of ISO filtered OLR anomaly for pIOD years. We notice that the convection initiates at lag 12 days (Fig. 5b) again over WEIO but slightly to the west of 60° E and slightly to the north of the equator. By lag 9 days, we see an elongated region of moderate convection from 60° E to the southern tip of India (Fig. 5c). The convection further intensifies, moving east. By lag 3 days, intense convection can be seen just to the south of India (Fig. 5e), and the convection moves further eastward before weakening by lead 6 days (Fig. 5h). Weak northward propagation from lag 0 days to lead 9 days is evident (Fig. 5f–i). One more notable difference between the pIOD and nIOD years evolution composites is that during pIOD years, most of the strong convection prefers to stay north of the equator (Fig. 5c–f). During nIOD years, the convection moves along the equator (Fig. 4c–f). Also, the strength of convection is generally weaker during pIOD years (not clearly visible in the Figs. 4 and 5 due to scale chosen to plot them). Comparing Figs. 4 and 5f–i, it is evident that northward propagations are weaker during pIOD years, as pointed out in Ajayamohan et al. (2008). To confirm this observed weakening of northward propagations (Figs. 4, 5) during pIOD years, we examined the individual evolution cycles from which the composites (Figs. 4, 5) are constructed for nIOD and pIOD years. The following algorithm is used to count the northward propagating events.

Algorithm:

Step 1: The day when area-averaged ISO filtered OLR anomaly is minimum *over the region 2.5° N – 7.5° N and 70° E – 95° E* is marked as day 0. This condition can be expressed as follows:

if $(OLR)_{n-1} > (OLR)_n < (OLR)_{n+1}$ then the nth day is taken as day 0 for the cycle.

Step 2: Check if the same condition in step 1 was met o*ver the region 17.5° N – 22.5° N and 70° E – 95° E within 10 – 20 day's period from day 0* marked in step 1. (Note that the region chosen in this step is north of the region selected in step 1)

Step 3: If the condition in step 2 associated with step 1 is satisfied, we count the event as a northward propagating event.

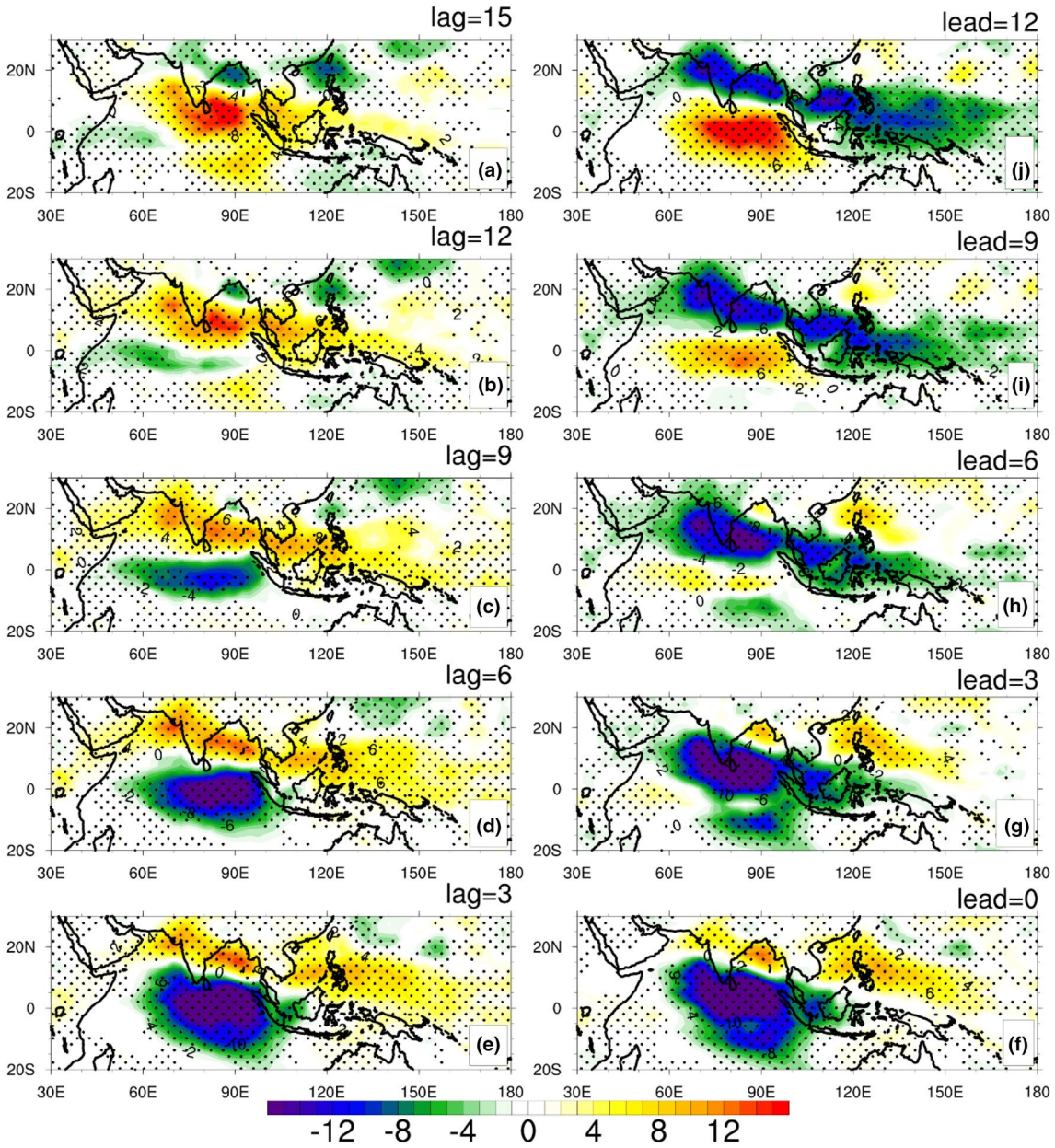

Fig. 4 Evolution composite of ISO filtered OLR anomalies (W/m^2) for nIOD years. The composite is constructed from 42 events across 10 nIOD years (Table 1), regions with significance level greater than 95% (using two tailed t test) are stippled

Using the above algorithm, we found that among 42 events across 10 nIOD years, 34 events (81%) propagated northward, while among 25 events across 7 pIOD years, only 7 (28%) propagated northward. The reduction in the number of northward propagating events during nIOD years from this algorithm against the 95% significance shown in the composite plot (Fig. 4) could be because of the longitudinal extent we selected in step 2 of the algorithm for calculating the average ISO filtered OLR anomaly. Sometimes the propagation characteristics are such that northward propagation can be seen in the Arabian Sea and with no propagation in the Bay of Bengal and vice versa. The OLR minima criteria (step 2) is not satisfied sometimes in these kinds of events. Thus, the algorithm described above does not pick those propagations. The significance tests (Figs. 4, 5) are done at each grid point rather than working with the area-averaged values as in the algorithm and, thus, are more robust. Nevertheless, the application of the algorithm confirms that the northward propagations are more prominent during nIOD years and weak during pIOD years.

As already discussed, though there is some difference in the structure of convection across contrasting IOD years,

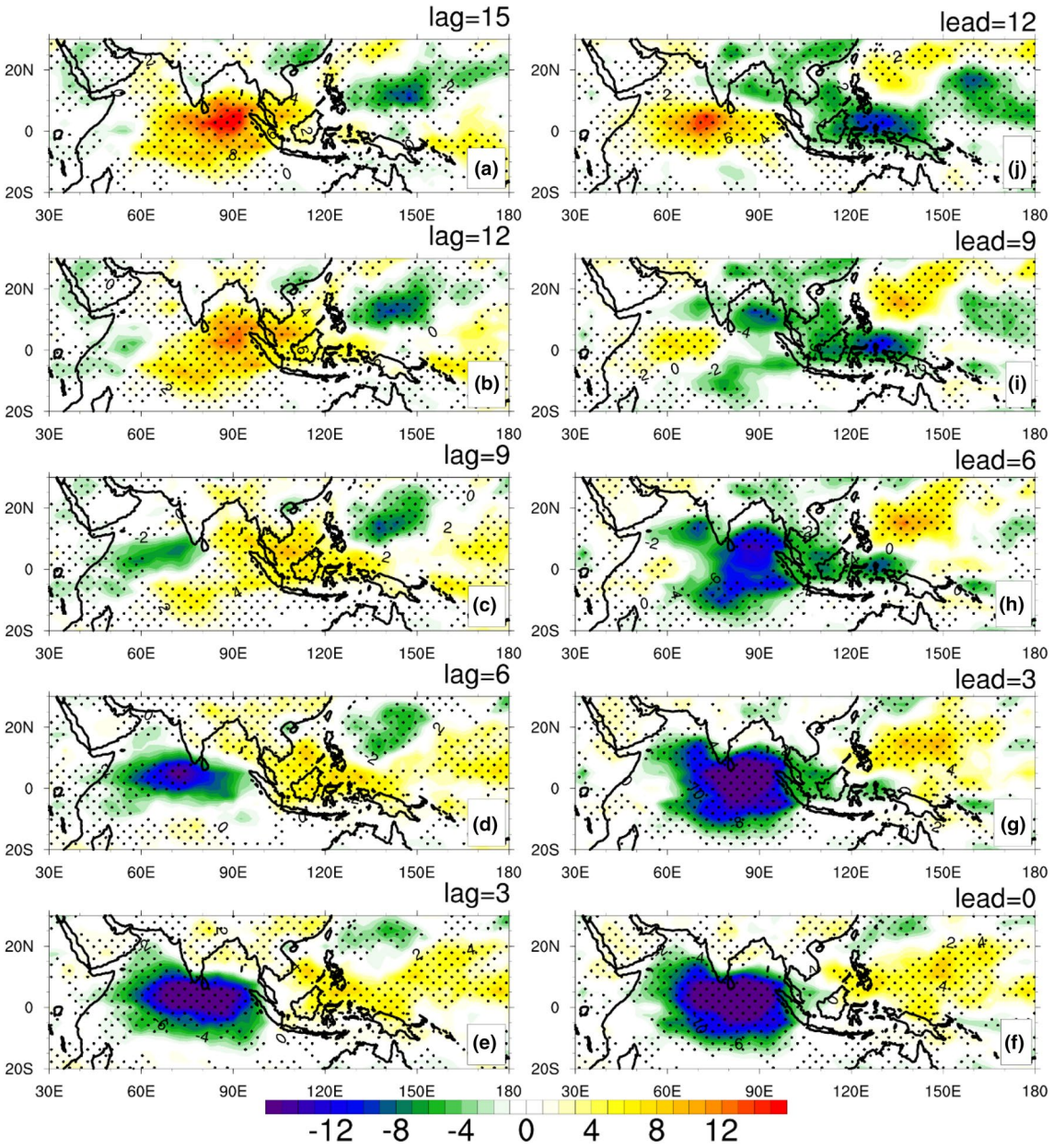

Fig. 5 Evolution composite of ISO filtered OLR anomalies (W/m^2) for pIOD years. The composite is constructed from 25 events across 7 pIOD years (Table 1), regions with significance level greater than 95% (using two tailed t test) are stippled

we here concentrate on lag 0 and ask the question, "Why were northward propagations weaker during pIOD years?" To answer this question, we resort to the "moisture mode" framework.

4 Moist entropy and its budget

The moist static energy (MSE) was used in several studies in the past for understanding the MJO propagation (e.g., Maloney 2009; Kiranmayi and Maloney 2011; Adames and Wallace 2015). In our analysis, we use moist entropy instead of MSE. The MSE is conserved by the parcel under the hydrostatic and moist adiabatic assumption, while the moist entropy is preserved by the parcel in a slow, moist/dry adiabatic process (Raymond and Fuchs 2009; Jiang et al. 2018).

The moist entropy following Raymond and Fuchs (2009) is given by,

$$S = T_R\left(C_{p_D} + r_v C_{pv}\right)\ln\left(\frac{T}{T_R}\right) - R_D T_R \ln\left(\frac{P_D}{P_R}\right) - r_v R_v T_R \ln\left(\frac{p_v}{e_{sF}}\right) + L_v r_v \quad (1)$$

where C_{pD}, R_D, p_D are specific heat, gas constant and pressure respectively of dry air, C_{pv}, R_v, p_v are specific heat, gas constant and vapor pressure respectively of water vapor, T is the temperature of the air in Kelvin, T_R is the reference temperature, which is 273.15 K, $r_v = \frac{q}{1-q}$ is the water vapor mixing ratio (q being specific humidity), L_v is the latent heat of vaporization taken as $2 \cdot 5 \times 10^6$ J/kg. The specific humidity is not directly available from the reanalysis-2 data set; thus, it was constructed from temperature (T), and relative humidity (RH) following Bolton (1980), the saturation vapor pressure (Bolton 1980) is given by,

$$e_s = 6.11 \exp\left(\frac{17 \cdot 67T}{T + 243.5}\right) \quad (2)$$

where T—temperature of air in degrees Celsius. Once the saturation vapor pressure (e_s) is obtained, the specific humidity (q) is constructed using,

$$q = 0.622 \frac{p_v}{p_t - p_v} \quad (3)$$

where p_v is the vapor pressure given by $p_v = RH \times e_s$.

According to Bolton (1980), Eq. (2) fits with an error of 0.1% for temperatures in the range of −30 °C to 35 °C. Nevertheless, we checked for the accuracy of this constructed specific humidity comparing with reanalysis-1 specific humidity data available. We found that the constructed values are in good agreement. The JJAS climatology of vertically integrated specific humidity between 1000 hpa level and 500 hpa level averaged over the region 10° S–30° N and 60° E–120° E has a root mean square error of 2.49 kg m^{-2}/day (6% of mean area-averaged specific humidity over the same region in reanalysis data). Having obtained all the data available for the construction of entropy from Eq. (1). We can write the entropy budget as:

$$\frac{\partial S}{\partial t} = -\bar{v} \cdot \nabla S - \omega \frac{\partial S}{\partial p} + F + Q \quad (4)$$

where the first term $(-\bar{v} \cdot \nabla S)$ on the RHS of Eq. (4) represents the horizontal advection, the second term $-\left(\omega \frac{\partial S}{\partial p}\right)$ corresponds to vertical advection, third term (F), and fourth term (Q) corresponds to the surface fluxes and radiative fluxes, respectively.

Since we are interested in intraseasonal oscillations of timescales 25–80 days (northward propagations), we integrate (mass-weighted) the above Equation from 1000 hpa level to 200 hpa level and apply ISO filter (Maloney 2009) giving:

$$\left[\frac{\partial S}{\partial t}\right]_{ISO} = \left[-\bar{v} \cdot \nabla S\right]_{ISO} - \left[\omega \frac{\partial S}{\partial p}\right]_{ISO} + \mathrm{F}_{ISO} + Q_{ISO} \quad (5)$$

where the terms within square bracket imply the vertical integration given by:

$$[a] = \int_{1000}^{200} a \frac{\mathrm{d}p}{g} \quad (6)$$

We show the spatial relationship between the convection and the moist entropy before looking at the entropy budget. The ISO filtered OLR and ISO filtered moist entropy anomalies corresponding to lag 0 days (Fig. 4) are shown in Fig. 6. The OLR and moist entropy anomalies are out of phase at lag 0 for both nIOD (Fig. 6a) and pIOD (Fig. 6b), however during pIOD years, the weak positive anomalies of entropy can be seen over peninsular India where the OLR anomalies are close to zero. Since OLR is used here as a

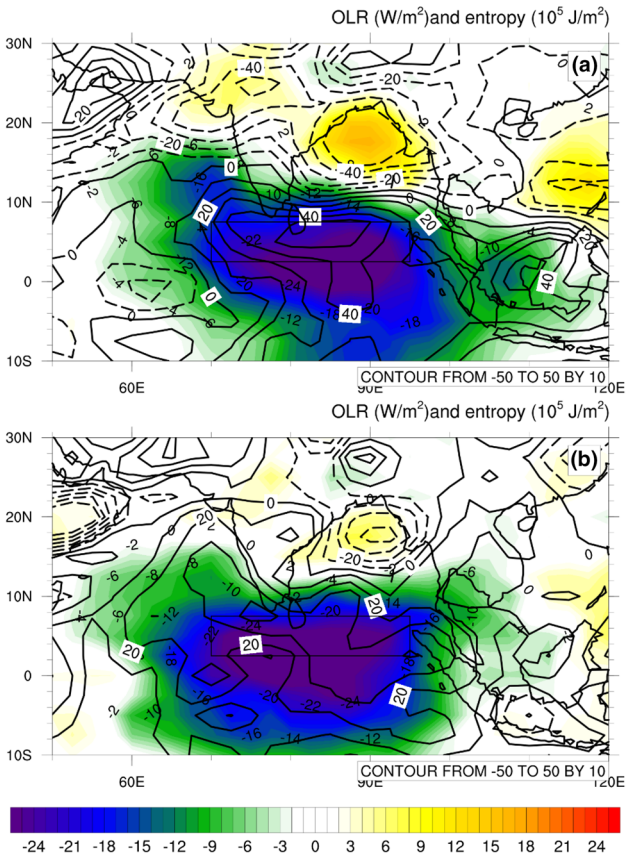

Fig. 6 Composite of ISO filtered OLR (colour shaded contours, W/m^2) and moist entropy (lined contours,10^5 J/m^2) anomalies for a) nIOD and b) pIOD years corresponding to the day of ISO OLR minima over region 2.5° N–7.5° N and 70° E–95° E (lag 0 days in Fig. 4) shown as rectangular box. The solid lined and dashed lines represent the positive and negative anomalies of moist entropy, respectively

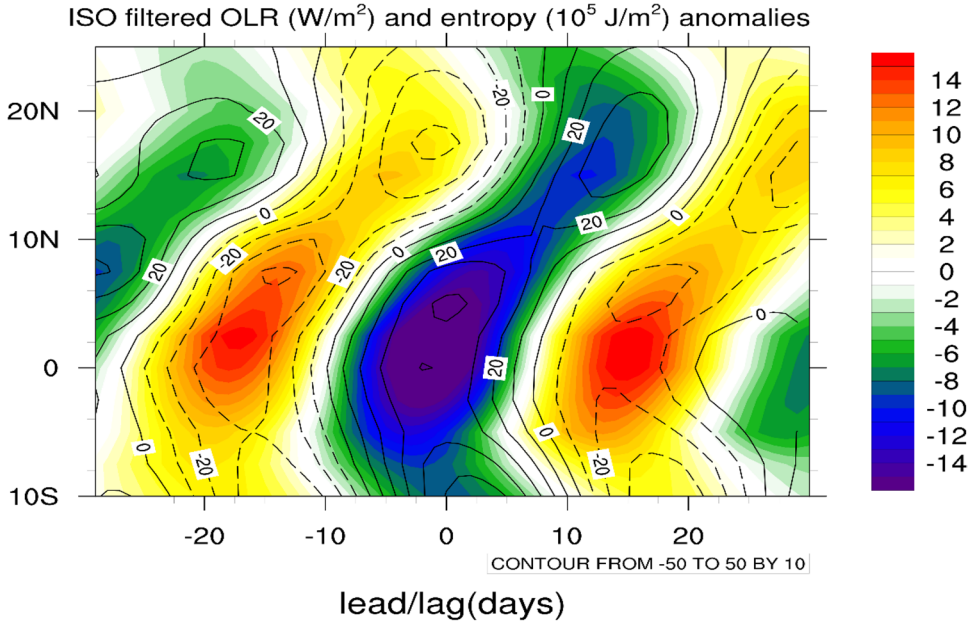

Fig. 7 Latitude-time composite evolution of ISO filtered OLR anomalies (colour shaded contours, W/m^2) and moist entropy anomalies (lined contours, 10^5 J/m^2) averaged across longitudes 70° E–95° E. Lag (days) corresponds to those shown in Fig. 4. The solid lined and dashed lines represent the positive and negative anomalies of moist entropy, respectively

proxy for rainfall, the moist entropy and rainfall will be in phase, as discussed in Jiang et al. (2018). The latitude-time plot of ISO filtered OLR, and moist entropy averaged across the longitudes 70° E–95° E is shown in Fig. 7. The ISO filtered moist entropy also propagates northward like the OLR, and the out of phase relationship between OLR and entropy is well demonstrated (Fig. 7).

Figure 8 shows terms in Eq. (5) when convection is centred at 5° N (lag 0 in Fig. 4) for nIOD years. Each term's average over the region 10° N–20° N, 70° E–95° E (to the north of convection centre) are printed on each panel's top. The tendency term ($\left[\frac{\partial S}{\partial t}\right]_{ISO}$, Fig. 8a) to the north of the convection centre is majorly controlled by the horizontal advection ($\left[-\overline{v}\cdot\nabla S\right]_{ISO}$, Fig. 8b), vertical advection ($\left[-\omega\frac{\partial S}{\partial p}\right]_{ISO}$, Fig. 8c) and the surface fluxes ($[F]_{ISO}$, Fig. 8d). The contributions from the radiative fluxes are small (Fig. 8e). While the horizontal advection tends to increase the entropy to the north of the convection centre, the other two terms try to decrease it. The vertical advection peaks over the topographic features like western ghats and Myanmar (Fig. 8c).

During pIOD years, in the budget of Eq. (5), the tendency term ($\left[\frac{\partial S}{\partial t}\right]_{ISO}$, Fig. 9a) to the north of the convection centre decreases considerably in comparison with nIOD years (Fig. 8a). The horizontal advection ($\left[-\overline{v}\cdot\nabla S\right]_{ISO}$) which is the major contributor to the tendency term during nIOD years is also significantly reduced during pIOD years (Fig. 9b). Even though magnitudes of vertical advection (Fig. 9d) and surface fluxes (Fig. 9c) reduced considerably, the tendency during pIOD is decreased majorly due to reduction in horizontal advection. Figure 10 shows the bar graph of the same entropy budget for nIOD and pIOD years. To understand the reason for this reduction in the horizontal advection term, we split Eq. (5) into zonal and meridional components as,

$$-\left[\overline{v}\cdot\nabla S\right]_{ISO} = -\left[u\frac{\partial S}{\partial x}\right]_{ISO} - \left[v\frac{\partial S}{\partial y}\right]_{ISO} \tag{7}$$

where the first and second terms on the RHS represents zonal advection and meridional advection, respectively. The major contribution to the horizontal advection comes from the zonal advection ($-\left[u\frac{\partial S}{\partial x}\right]_{ISO}$) term, and there is a reduction in the zonal advection term during pIOD years. There is also a considerable contribution from the meridional advection term ($-\left[v\frac{\partial S}{\partial y}\right]_{ISO}$) in nIOD years (Fig. 11a), but the contribution from meridional advection during pIOD years (Fig. 11b) is negligible. The reduction in the zonal advection and the meridional advection stands close to 5 W/m^2 and 8 W/m^2 respectively.

The smaller budget terms at lag 0 days during pIOD years could result from the phase relationship difference across contrasting IOD years. To investigate this, we examined the phase relationship between the horizontal

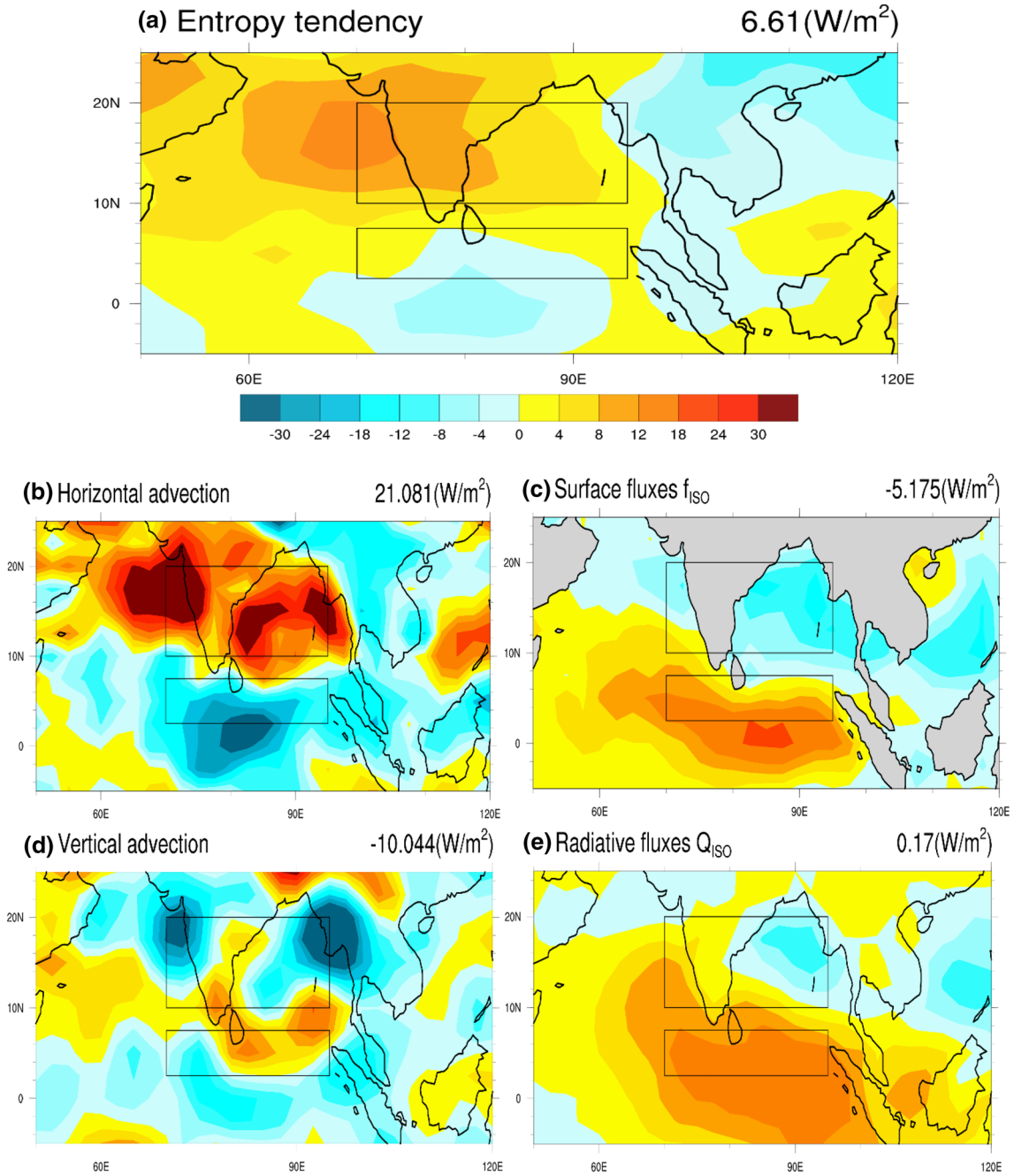

Fig. 8 Lag 0 patterns of **a** entropy tendency $\left[\frac{\partial S}{\partial t}\right]_{ISO}$, **b** horizontal advection $\left[-\overline{v}\cdot\nabla S\right]_{ISO}$, **c** surface fluxes F_{Iso}, **d** vertical advection $\left[-\omega\frac{\partial S}{\partial p}\right]_{ISO}$, and **e** radiative fluxes Q_{ISO}, all in W/m^2 for nIOD years. The region 2.5° N–7.5° N and 70° E–95° E (lower rectangle) shows the region over which ISO convection (OLR) is maximum (minimum) on lag 0 day, the average of each term over the 10° N–20° N and 70° E–95° E (upper rectangle) region are printed on top right of each figure

advection ($-\left[\overline{v}\cdot\nabla S\right]_{ISO}$) term and the OLR/rainfall, by constructing a composite lag-phase diagram of horizontal advection and its components along with the OLR (all ISO filtered) averaged over the region 10° N–20° N, 70° E–95° E. Figure 12 shows the composite lag phase diagram for all nIOD and pIOD events, lag 0 corresponds to the day when the OLR minima is centered at at 5° N. The amplitudes of oscillation of all the variables are much smaller during pIOD years (Fig. 12b) in comparison with nIOD years (Fig. 12a). The maxima in the horizontal advection for nIOD years coincidentally occurs close to

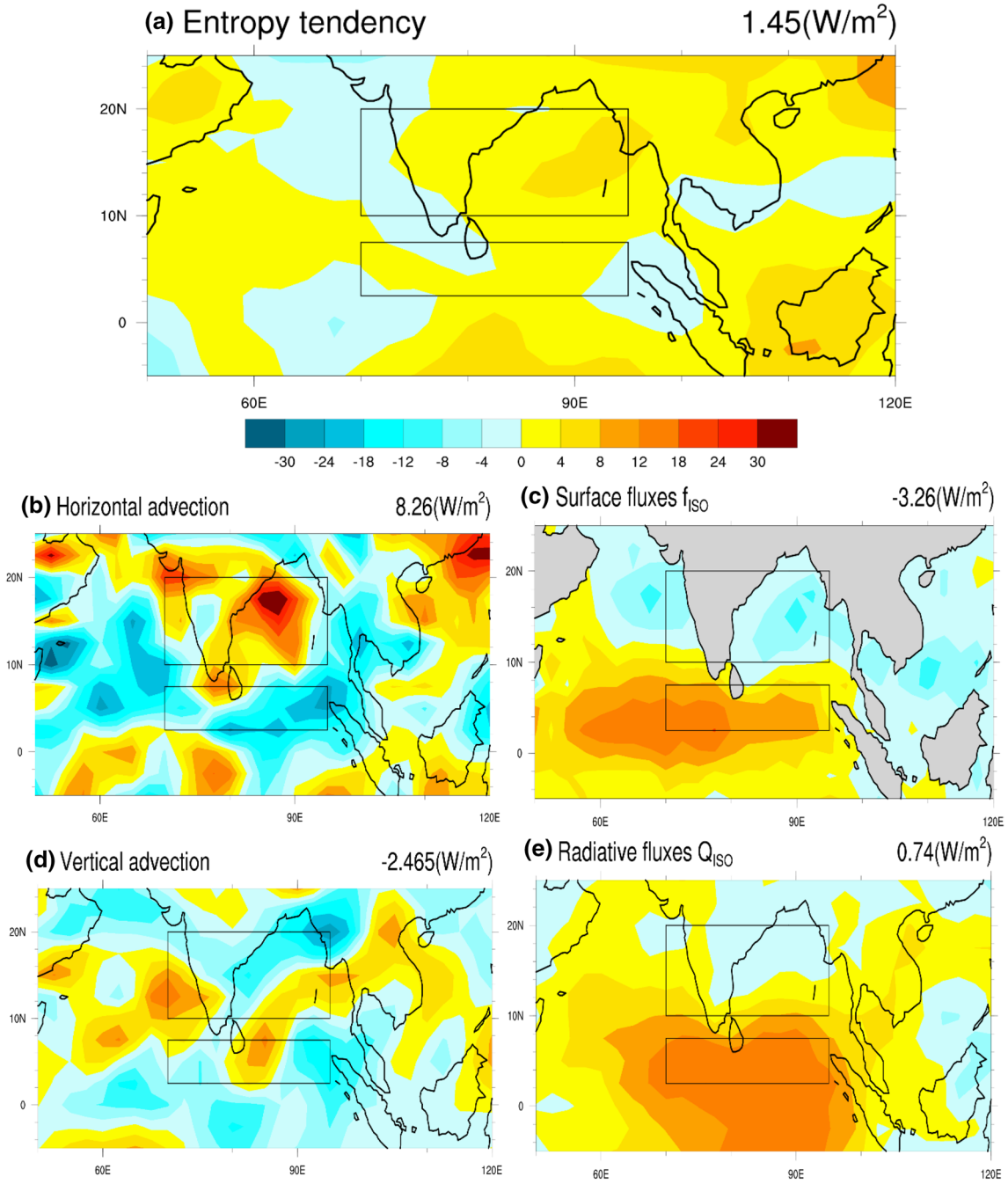

Fig. 9 Same as Fig. 8 but for pIOD years

lag 0 days, and for pIOD years the maxima occur close to lead 2 days. Thus, the horizontal advection enhances moisture in the atmosphere to the north of the convection centre during both nIOD and pIOD years. Nevertheless, during pIOD years the amplitude is smaller, and both the zonal and meridional advection weakens, with the contribution from the latter being almost zero. Also, during nIOD years, the minima (maxima) in OLR (rainfall) over the region 10° N–20° N, 70° E–95° E occurs close to lag 10 days (Fig. 12a), which is consistent with 1°/day speed of propagation as observed in previous studies (e.g., Yasunari 1979; Krishnamurti and Subramanyam 1982; Jiang et al. 2004).

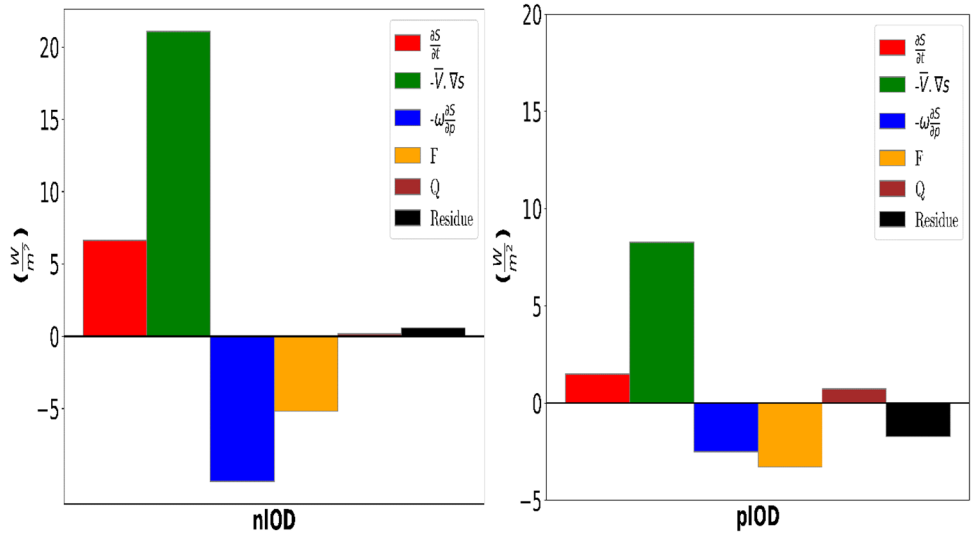

Fig. 10 Entropy budget (the average over the region 10° N–20° N, 70° E–95° E, W/m^2) pertaining to Eq. (5) on lag 0 for nIOD (left) and pIOD (right) years

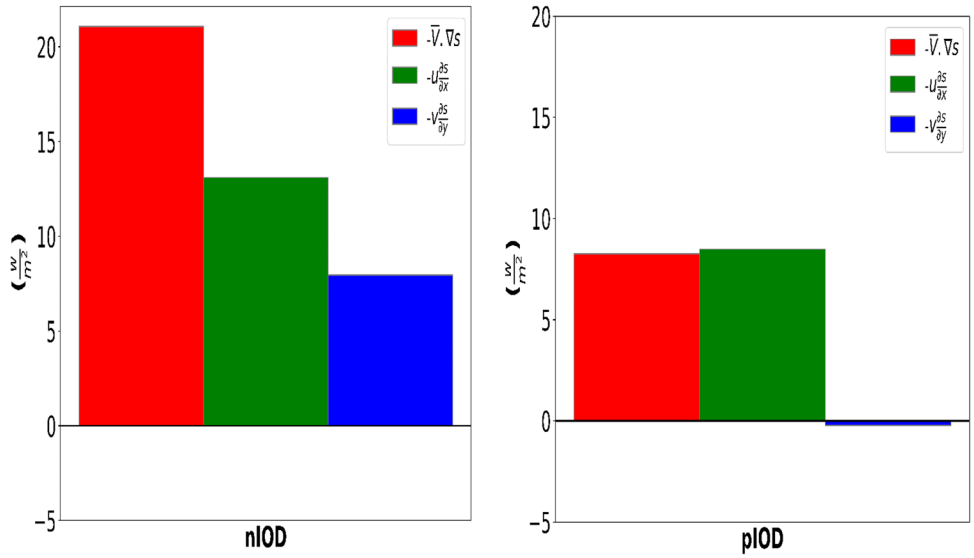

Fig. 11 The horizontal advection budget (the average over the region 10° N–20° N, 70° E–95° E, W/m^2) pertaining to Eq. (7) for nIOD years (left) and pIOD years (right) corresponding to lag 0 (Figs. 4, 5)

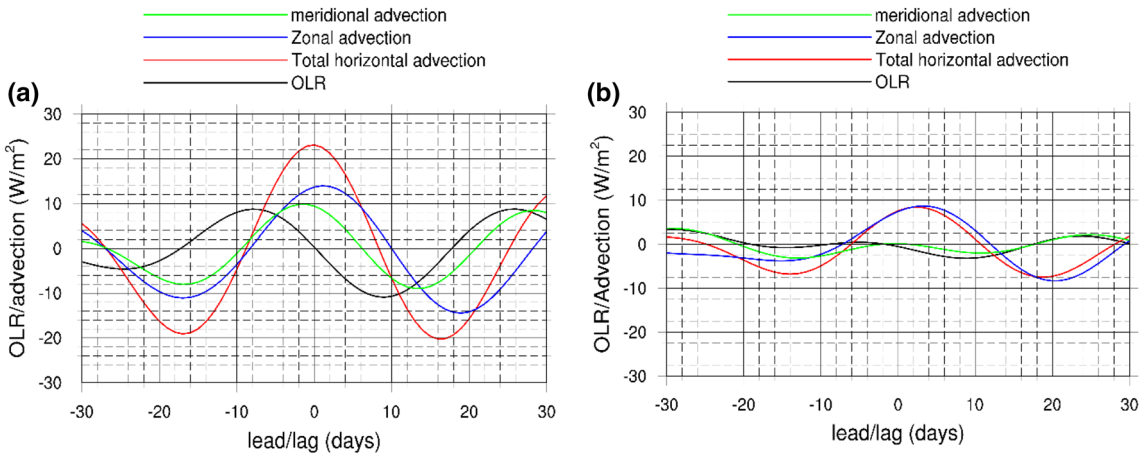

Fig. 12 The composite phase relationship between the horizontal advection (averaged over the region 10° N–20° N, 70° E–95° E) and OLR, both in W/m^2 for **a** nIOD (left), **b** pIOD (right) years. Lag 0 corresponds to the convection centred at 5° N (Fig. 6)

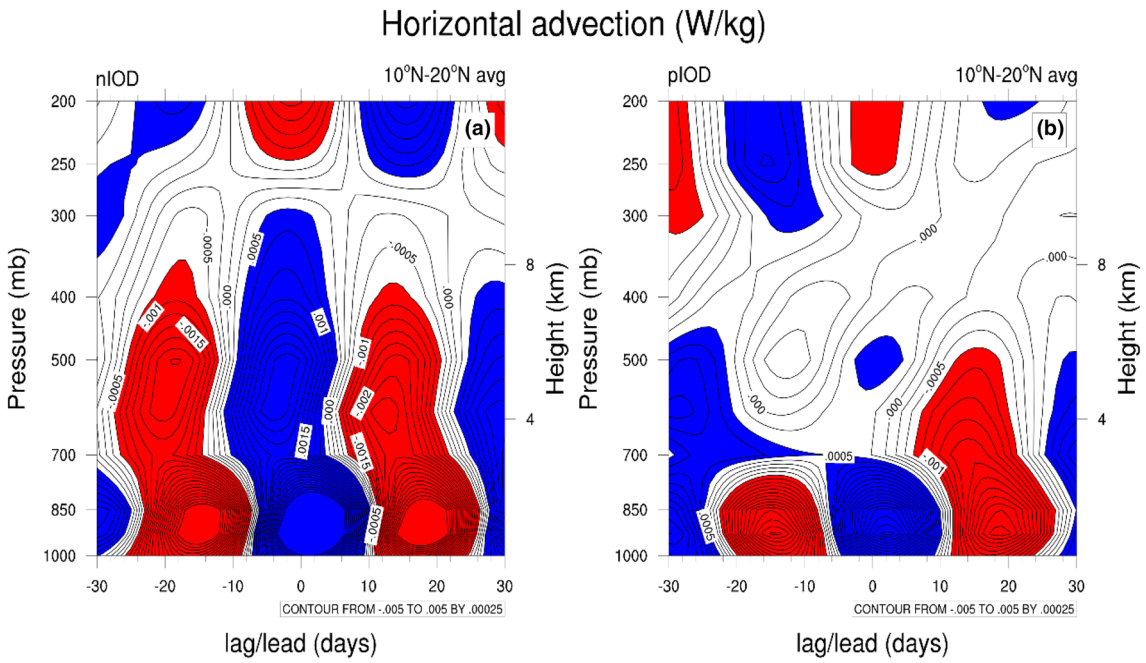

Fig. 13 Composite vertical structure of ISO filtered horizontal advection ($-\overline{v} \cdot \nabla S$, W/kg) (averaged across 10° N–20° N) for **a** nIOD and **b** pIOD years, values above 5×10^{-4} W/kg are shaded in blue and values below -5×10^{-4} W/kg are shaded in red. X axis shows the lead/lag in days and Y axis shows pressure levels in millibar

4.1 Vertical structure of horizontal advection

To understand the smaller amplitude of horizontal advection during pIOD years, the horizontal advection's vertical structure across the contrasting IOD years averaged over the region 10° N–20° N, 70° E–95° E (region to the north of convection centre at lag 0 days) is examined at various lag/lead times (Fig. 13). During nIOD years (Fig. 13a), there exist two local maxima/minima in horizontal advection $\left(-\overline{v} \cdot \nabla S\right)$ one in the lower troposphere between 1000 and 850 hpa levels, and the other in the middle troposphere between 600 and 400 hpa levels. The magnitude of the lower troposphere maximum is larger ($>0.0075\ \frac{w}{kg}$) than that of the magnitude of maximum in the middle troposphere (just above $0.0025\ \frac{w}{kg}$). While the lower troposphere maximum/minimum can be seen in pIOD years (but smaller magnitudes), the middle troposphere undergoes remarkable change (Fig. 13b). Though the secondary maximum can be seen in the middle troposphere during pIOD years, the magnitude of the same (close to $0.0005\ \frac{w}{kg}$) is much smaller than the same for nIOD years.

To understand what causes this change, we examined the contribution of zonal $(-u\frac{\partial S}{\partial x})$ and meridional $(-v\frac{\partial S}{\partial y})$ advection terms to the vertical structure of horizontal advection. In Fig. 14, vertical structures of zonal and meridional advection leading to Fig. 13 are separated and plotted. During both pIOD and nIOD years, the meridional advection helps in moistening the boundary layer and lower troposphere up to 800 hpa (Fig. 14c, d), but the vertically integrated value on day 0 remains small during pIOD events (Figs. 11, 12) because of the smaller magnitude of meridional advection along with negative contribution at middle and higher troposphere (Fig. 14d). The major difference, as seen in Fig. 14, though, occurs in the zonal (Fig. 14a, b) advection which helps to moisten the middle troposphere and a part of the lower troposphere close to 850 hpa level. A strong moistening signal can be seen during nIOD years (Fig. 14a) with a primary maximum close to 850 hpa level and secondary maximum close to 600 hpa, whereas the signal is weaker in pIOD years (Fig. 14b). Though the two maxima are still present, their magnitudes, especially the one at 850 hpa level, is much smaller than nIOD years. Thus, despite the lower troposphere's moistening by meridional advection to the north of the convection centre during pIOD years, zonal advection's contribution is considerably smaller, leading to weaker entropy advection above 700 hpa level (Fig. 13b), to the north of convection centre.

The same conclusion can be obtained from the latitude–height structure of zonal and meridional advection at lag 0 days shown in Fig. 15. The zonal advection in nIOD years helps in moistening the middle troposphere and a part of the lower troposphere close to 850 hpa level (Fig. 15a), between 10° N and 20° N. The zonal advection is much weaker during pIOD years (Fig. 15b), and 850 hpa maximum is absent. The moistening of the boundary layer and

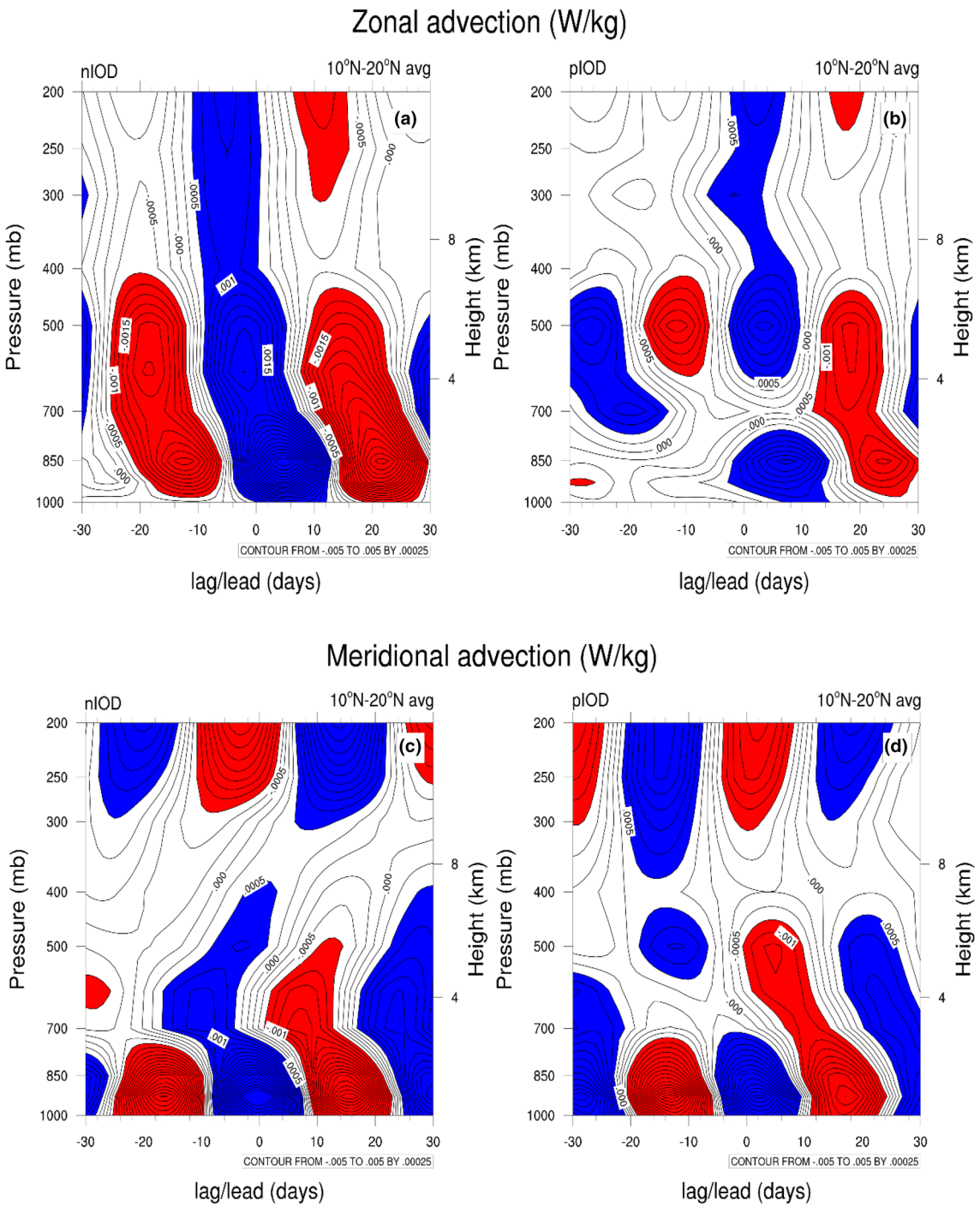

Fig. 14 Contributions of zonal $(-u\frac{\partial S}{\partial x})$ and meridional advection $(-v\frac{\partial S}{\partial y})$ (W/kg) to the vertical structure of horizontal advection (Fig. 13) for **a**, **c** nIOD and **b**, **d** pIOD years, like Fig. 13 values above 5×10^{-4} W/kg are shaded in blue and values below -5×10^{-4} W/kg are shaded in red. X axis shows the lead/lag in days and Y axis shows pressure levels in millibar

lower troposphere by the meridional advection is present in both the contrasting IOD years; the signal is stronger during nIOD years (Fig. 15c) than during pIOD years (Fig. 15d). This structure leads to strong moistening of the lower and middle troposphere to the north of the convection centre during the nIOD year (Fig. 15e), while the moistening is weaker during pIOD years (Fig. 15f).

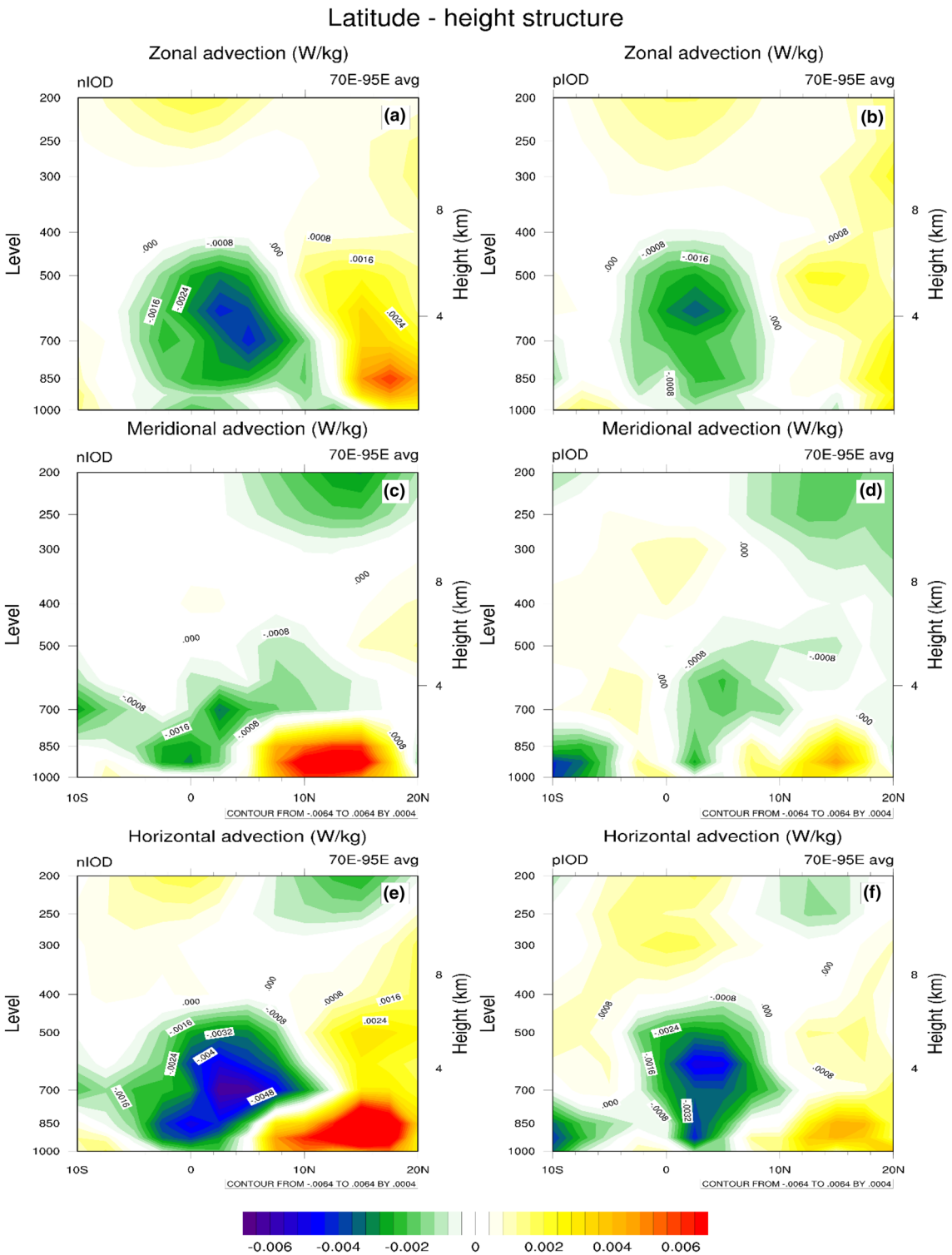

Fig. 15 Latitude-height structure of ISO filtered **a**, **b** zonal $(-u\frac{\partial S}{\partial x})$, **c**, **d** meridional $(-v\frac{\partial S}{\partial y})$ and **e**, **f** total horizontal $(-\overline{v}\cdot\nabla S)$ advection anomalies (W/kg) respectively (averaged across 70° E–95° E) for nIOD (left) and pIOD (right) year's corresponding to lag 0 days. X-axis shows the latitude and Y axis the pressure levels in millibar

4.2 Horizontal advection budget

Having understood the relative roles of zonal and meridional advection in the vertical structure of horizontal advection during nIOD and pIOD years, we can ask the question, "what are the processes that regulate the horizontal advection?" to answer this question, we can split the meridional and zonal advection into respective components (Maloney 2009) as,

$$\left[v\frac{\partial S}{\partial y}\right]_{ISO} \approx \left[\overline{v}\frac{\partial S'}{\partial y}\right]_{ISO} + \left[v'\frac{\partial \overline{S}}{\partial y}\right]_{ISO} + \left[v'\frac{\partial S'}{\partial y}\right]_{ISO} \quad (8)$$

$$\left[u\frac{\partial S}{\partial x}\right]_{ISO} \approx \left[\overline{u}\frac{\partial S'}{\partial x}\right]_{ISO} + \left[u'\frac{\partial \overline{S}}{\partial x}\right]_{ISO} + \left[u'\frac{\partial S'}{\partial x}\right]_{ISO} \quad (9)$$

where the terms with bars $(\overline{u}, \overline{v}, \overline{S})$ represent 80-day running means, while the prime terms (u', v', S') represent a deviation from the mean. These perturbations contain both high frequency (less than 25 days) and low frequency (80–25 days) perturbations. Later in Sect. 4.2.2, we show that the contribution to the budget from the high-frequency terms is negligible.

4.2.1 Meridional advection budget

The meridional advection budget (Eq. (8)) for nIOD and pIOD years over the region 10° N–20° N, 70° E–95° E at various lag/lead times are shown in Fig. 16. During nIOD years, all the terms on RHS of Eq. (8) contribute equally to the budget at lag 0 days (Fig. 16a). But, during pIOD years, the contributions from the $v'\frac{\partial \overline{S}}{\partial y}$, $\overline{v}\frac{\partial S'}{\partial y}$ and $v'\frac{\partial S'}{\partial y}$ terms reduce approximately by 2.5 W/m^2, 1.5 W/m^2 and 4 W/m^2, respectively. Since the strong moistening from the meridional advection is limited to the boundary layer and lower troposphere below 850 hpa (Fig. 14c, d), we have also examined the advection budget for the lower troposphere (1000–850 hpa) (shown in Fig. S3 in the supplementary material to the manuscript). Though there is a reduction in meridional advection in the lower troposphere as well during pIOD years (Fig. S3(b)) in comparison with nIOD years (Fig. S3(a)), the reduction stands close to 3 W/m^2, much smaller compared to the reduction in total meridional advection budget (1000–200 hpa) shown in Fig. 16. Also, comparing Figs. 16 and S3, we see that the main difference between the lower tropospheric advection budget (1000–850 hpa) and the total advection budget (1000–200 hpa), in nIOD years is the presence of strong $v'\frac{\partial S'}{\partial y}$ anomalies in the atmosphere above 850 hpa level during nIOD years (Fig. 16(a) and Fig. S3(a)). The difference between $v'\frac{\partial S'}{\partial y}$ term in the lower troposphere (1000–850 hpa), and the total atmosphere (1000–200 hpa) is smaller during pIOD years (Fig. 16b and Fig. S3(b)). Thus, to ascertain the reason for the difference in $v'\frac{\partial S'}{\partial y}$ term across contrasting IOD years the meridional wind perturbation maps at levels 700 hpa, 600 hpa and 500 hpa (not shown here) were examined. It has been found that meridional wind perturbation turns northerly over southern peninsular India with the strongest northerly perturbations over Southeast Arabian Sea due to the presence of strong Rossby vortex lobes (discussed in detail in Sect. 5) during nIOD years. In contrast, the wind perturbations are southerly over southern peninsular India during pIOD years due to weak Rossby vortex lobes. Also, from Fig. 6 we see that there exists a strong meridional gradient of entropy perturbation $(\frac{\partial S'}{\partial y})$ dur-

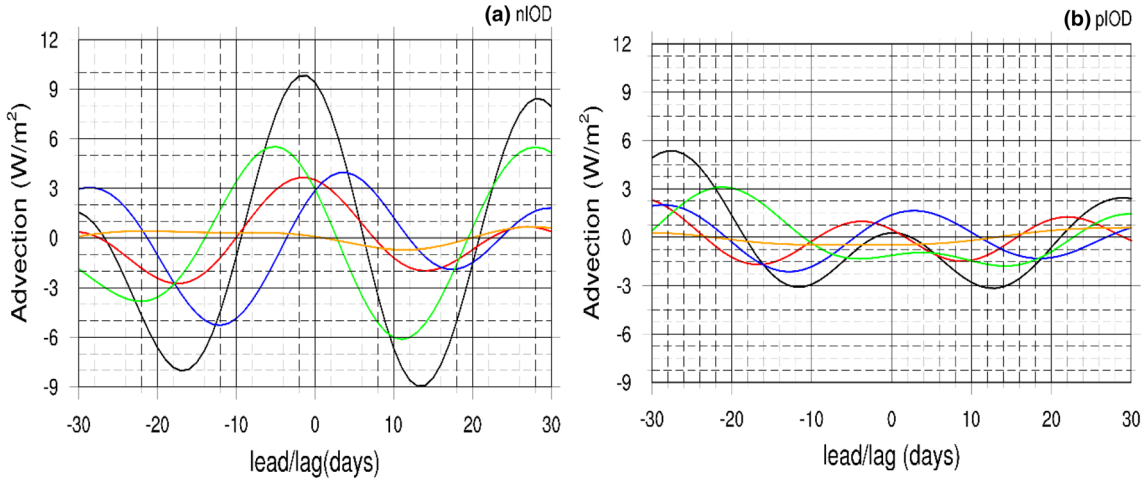

Fig. 16 Meridional advection (vertically integrated between 1000 and 200 hpa, W/m^2) budget pertaining to Eq. (8) for **a** nIOD and **b** pIOD over the region 10° N–20° N, 70° E–95° E, the black curve shows $v\frac{\partial S}{\partial y}$, the red curve shows $v'\frac{\partial \overline{S}}{\partial y}$, the blue curve shows $\overline{v}\frac{\partial S'}{\partial y}$, the green curve shows $v'\frac{\partial S'}{\partial y}$, and the orange curve shows the residue term. Lag 0 corresponds to the day in Fig. 6

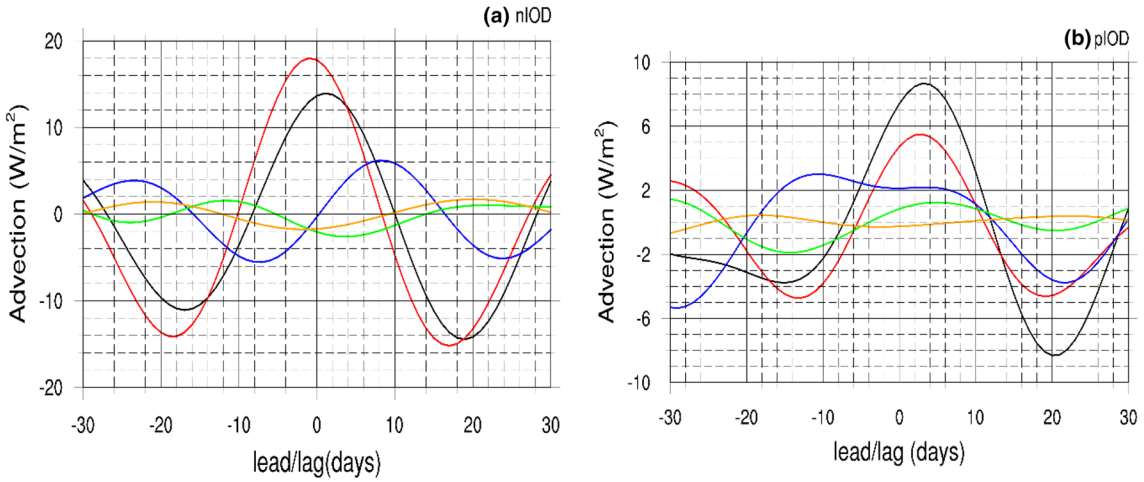

Fig. 17 Zonal advection (vertically integrated between 1000 and 200 hpa, W/m^2) budget pertaining to Eq. (9) for **a** nIOD and **b** pIOD over the region 10° N–20° N, 70° E–95° E, the black curve shows $u\frac{\partial S}{\partial x}$, the red curve shows $u'\frac{\partial S}{\partial x}$, the blue curve shows $\overline{u}\frac{\partial S'}{\partial x}$, the green curve shows $u'\frac{\partial S'}{\partial x}$, and the orange curve shows the residue term. Lag 0 corresponds to the day in Fig. 6. (Note that scales of Y axis are different for figures a and b)

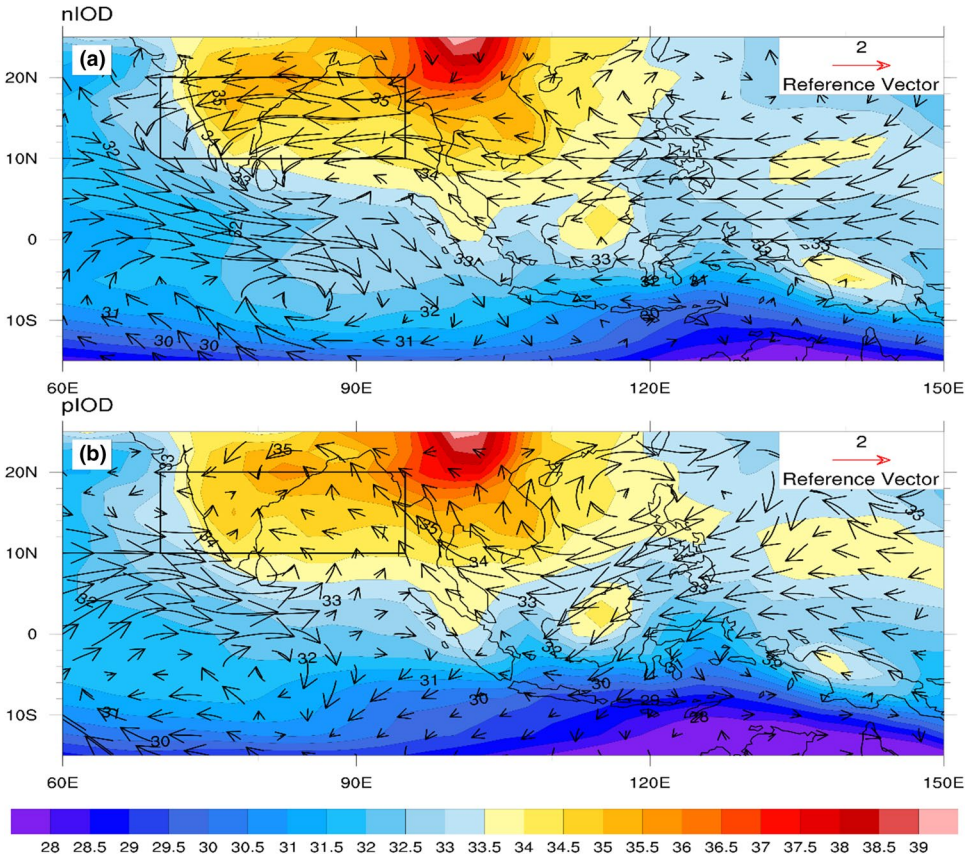

Fig. 18 The background (JJAS) entropy (vertically integrated between 925 and 500 hpa levels, 10^7 J/m^2) overlayed by 850 hpa wind perturbations (m/s) vectors corresponding to lag 0 days (Fig. 6) for **a** nIOD and **b** pIOD years. The rectangular box represents the region 10° N–20° N, 70° E–95° E. The reference vectors are shown on top right of each panel

ing nIOD years as compared to pIOD years. These two factors lead to a reduction in the $v' \frac{\partial S'}{\partial y}$ term by 4 W/m^2 as discussed earlier (Fig. 16).

4.2.2 Zonal advection budget

Figure 17 shows the zonal advection budget (Eq. (9)) for nIOD and pIOD events over the region 10° N–20° N, 70° E–95° E at various lag/lead times. The contribution to the zonal advection during both nIOD and pIOD years is dictated by the advection of mean entropy by perturbed zonal wind ($u' \frac{\partial \bar{S}}{\partial x}$) term (Fig. 17a, b). The contributions from $\bar{u} \frac{\partial S'}{\partial x}$ and $u' \frac{\partial S'}{\partial x}$ terms to the zonal advection during both nIOD and pIOD years are negligible in comparison with the $u' \frac{\partial \bar{S}}{\partial x}$ term. Thus, the reduction in the zonal advection between contrasting IOD years can be entirely attributed to the reduction in $u' \frac{\partial \bar{S}}{\partial x}$ term, which reduces approximately by 12 W/m^2 (Fig. 16a, b) during pIOD years in comparison with the nIOD years. This value is three times the magnitude of the largest contributing term ($v' \frac{\partial S'}{\partial y}$) that causes the difference in meridional advection term during contrasting IOD years. The major difference in the zonal advection ($\left[u \frac{\partial S}{\partial x}\right]_{ISo}$) term during contrasting IOD years should either come from the different mean entropy gradients ($\frac{\partial \bar{S}}{\partial x}$) or the perturbation of zonal velocities (u') across contrasting IOD years. To understand which of these two terms is responsible for the smaller amplitude of zonal advection during pIOD years, we have examined the perturbed velocity vectors at 850 hpa level corresponding to lag 0 days along with the JJAS mean structure of vertically integrated lower to middle troposphere (925–500 hpa) entropy for nIOD and pIOD years (Fig. 18). It is evident from Fig. 18 that the mean structure of entropy ($\bar{S}$) over the Asian summer monsoon region does not differ much across contrasting IOD years, the major difference between the two is the presence of strong easterly wind perturbations (u') during nIOD years between latitudes 10° N–20° N at lag 0 days (Fig. 18a), those perturbations are much weaker during pIOD years (Fig. 17b). These weaker wind perturbations result in very weak zonal advection to the north of the convection centre (Figs. 14b, 15b) during pIOD years in comparison with nIOD years (Figs. 14a, 15a). This weaker zonal advection, along with weaker meridional advection (Sect. 4.2.1), leads to weaker tendencies of entropy (moisture build-up) and thus weaker northward propagations during pIOD years.

Note that the perturbation term in $u' \frac{\partial \bar{S}}{\partial x}$ contains all the frequencies within 0–80 days timescales. We can further approximate the perturbation term as the sum of high-frequency and low-frequency terms as,

$$u' \approx u_{lf} + u_{hf} \tag{10}$$

where *lf*—low-frequency mode corresponds to the periodicities of 25–80 days, and *hf*—high-frequency mode corresponds to 10–25 days. These two timescales are considered dominant periodicities in ISO, e.g., Yasunari (1979) and Karmakar et al. (2017). Thus, the term $u' \frac{\partial \bar{S}}{\partial x}$ can be written as:

$$u' \frac{\partial \bar{S}}{\partial x} \approx u_{lf} \frac{\partial \bar{S}}{\partial x} + u_{hf} \frac{\partial \bar{S}}{\partial x} \tag{11}$$

The budget pertaining to Eq. (11) is shown in Fig. 19. The dominance of low-frequency zonal wind can be seen. Thus, the major difference in the zonal advection between nIOD and pIOD events is caused by the weaker zonal wind

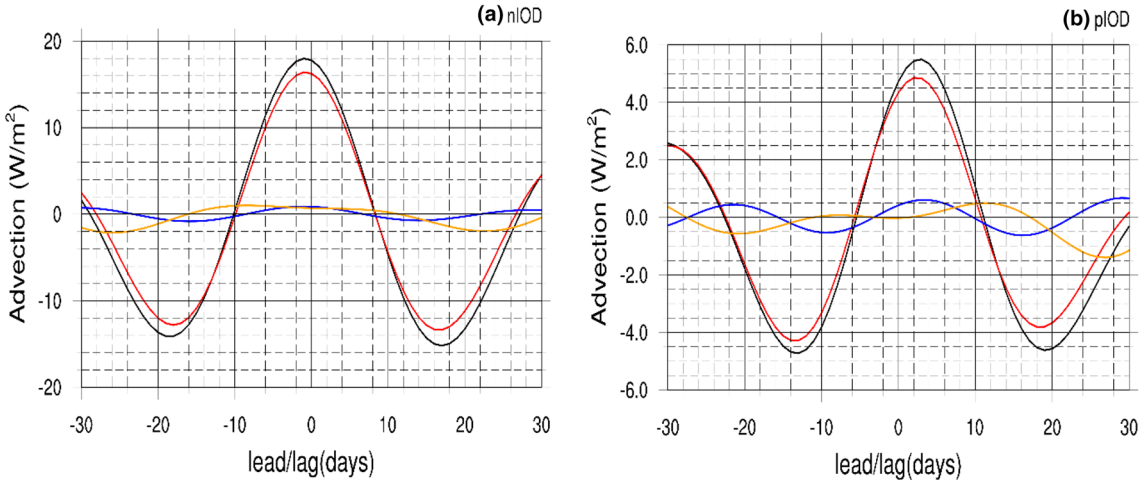

Fig. 19 Budget of ISO filtered $u' \frac{\partial \bar{S}}{\partial x}$ (vertically integrated between 1000 and 200 hpa) for **a** nIOD and **b** pIOD years over the region 10° N–20° N, 70° E–95° E, the black curve shows $u' \frac{\partial \bar{S}}{\partial x}$, red and blue curves show $u_{lf} \frac{\partial \bar{S}}{\partial x}$ and $u_{hf} \frac{\partial \bar{S}}{\partial x}$ respectively, and the orange curve shows the residue (Eq. (11)), lag 0 corresponds to day in Fig. 6. (Note that scales on Y-axis are different for **a** and **b**)

perturbations at 25–80 days timescales. In fact, the low-frequency wind at 850 hpa level on lag 0 days looks almost the same as shown in Fig. 18a for nIOD years (not shown here). Thus, the reduction in the horizontal advection is dominated by the $u' \frac{\partial \bar{S}}{\partial x}$ term and the reason for the reduction being the weaker zonal wind perturbations during pIOD years (Fig. 18).

5 Possible mechanism for weaker propagations during pIOD years

Having understood the reasons for weaker northward propagations in pIOD years, we propose the following mechanism for the weakening: we realized that the primary contributor for weaker propagations during pIOD years is the weaker zonal wind perturbations. The perturbed wind structure for nIOD (Fig. 18a) appears like a Gill-type response (Gill 1980) to symmetric convective heating about the equator, with two cyclonic vorticities (Rossby wave lobes) to the northwest and the southwest of convection centre/heating, easterly winds to the east and the north, and westerly winds to the west of convection centre. But during pIOD years (Fig. 18b), weak vortices can be seen leading to weak easterly wind perturbations to the north of the convective centre.

What causes the weakening of the Rossby Wave lobe? The weakening of the Rossby wave lobe can be caused by (a) difference in the background circulation and moisture (Chen and Wang 2021; Jiang et al. 2018) across contrasting IOD years, or (b) the difference in the structure and/or strength of the convective heating, as it is responsible for the generation of Rossby wave lobes (Gill 1980). Recently, Chen and Wang (2021), using the K-means algorithm, found 3 clusters of ISO, namely the canonical, the northward dipole and the eastward expansion. The first two clusters exhibit northward propagation, and eastward expansion clusters show no northward propagation. We observed that their canonical cluster looks like our nIOD propagations (Fig. 4), but the similarity ends there; the pIOD propagations do not appear like any of the clusters discussed in their work. Chen and Wang (2021) understood that the background zonal wind shear is stronger, and the low-level moisture is higher over Southeast Asia for northward dipole and canonical clusters leading to northward propagation.

The background zonal wind shear is responsible for generating barotropic vorticity to the north of the convection centre in the presence of baroclinic divergence (Jiang et al. 2004). Also, the mean moisture pattern plays an essential role in northward propagation (Jiang et al. 2018). Thus, we examined the difference in background states across contrasting IOD years. The background zonal wind shear is calculated as the difference in the zonal wind speeds at 850 hpa level and 200 hpa level averaged from May to October each year. The magnitude of maximum background zonal wind shear is highest for nIOD years (25.19 m/s) and lowest for pIOD years (22. 45 m/s) (Fig. S4 (a) in supplement), but still substantial. The difference in the background wind shear between nIOD and pIOD years is 2.74 m/s. However, the difference in maximum wind shear between neutral years and pIOD years is just 1.8 m/s [note that these differences are much less than the difference between clusters discussed in Chen and Wang (2021)]. Given that even neutral years have northward propagations, the shear difference between neutral and pIOD years is small to explain the weakening of northward propagations. Also, the background humidity is slightly higher over southeast Asia during the pIOD years in comparison with nIOD years (Fig. S4(b) in supplement). Thus, the difference in the background state may not be responsible for the weakening of northward propagations in pIOD years.

The other factor responsible for weaker Rossby wave lobes is the difference in the convective heating structure and/or strength during ISO events across contrasting IOD years. Figure 20 shows the structure and the strength of convective heating at lag 5 days. For nIOD years (Fig. 20a), the negative OLR anomalies (which implies convective heating) are present on either side of the equator and are confined mainly to EEIO, Sumatra and Borneo. During pIOD years (Fig. 20b), strong convective heating is primarily confined to the north of the equator. Also, the negative OLR anomalies (implying convection) are strong over warm waters (Fig. 2a) of WEIO and Central Equatorial Indian Ocean (CEIO) with weak anomalies over EEIO, Sumatra and to the east of Sumatra. This difference in convective heating structure and/or strength generates different equatorial wave responses across contrasting IOD years with stronger (weaker) Rossby wave during nIOD (pIOD) years resulting in strong (weak) northward propagation of ISO.

The difference in convective heating structure and strength (Fig. 20) between nIOD and pIOD years can be explained by referring to mean SST anomalies (Fig. 2) as follows. During nIOD years, positive SST anomalies can be seen on either side of the equator (Fig. 2b); this strengthens the positive SST gradient between WEIO and EEIO on either side of the equator. This positive SST gradient helps destabilize the boundary layer to the east of the ISO convection centre on either side of the equator through surface convergence (Lindzen and Nigam 1987), leading to a near symmetric convection structure about the equator as convection moves eastward initially. During pIOD years, the negative SST anomalies are confined mainly to the south of the equator (Fig. 2a), while positive anomalies are located to the north of the equator. Thus, strengthening the positive SST gradient to the north of the equator and flattening the SST gradient to the south of the equator. This SST structure makes the atmosphere to the north of the equator to be

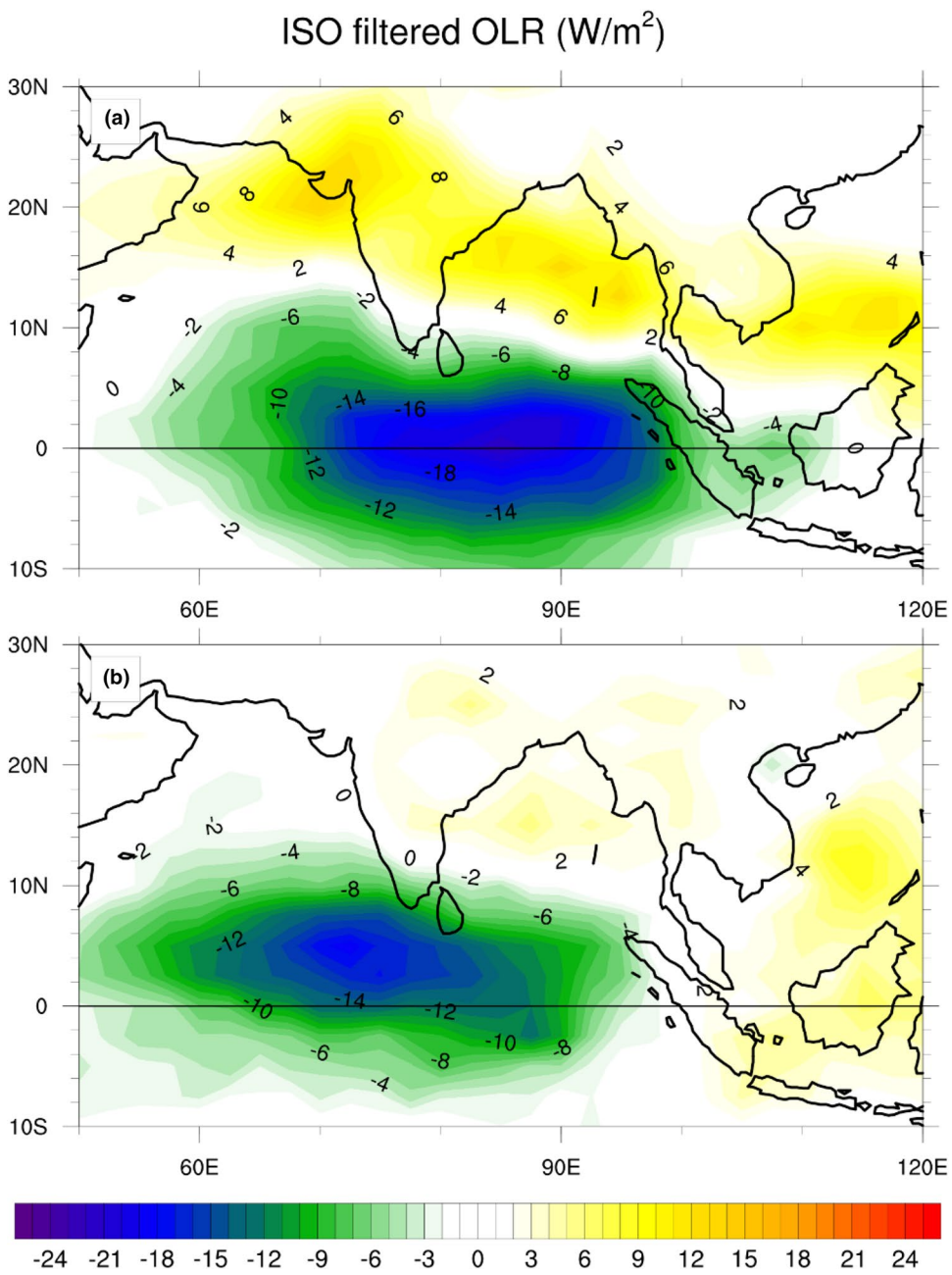

Fig. 20 ISO filtered OLR anomaly (W/m^2) pattern corresponding to lag 5 days showing the pattern of Intraseasonal convective heating structure for **a** nIOD and **b** pIOD years. The black bold lines show the equator

unstable and confines the strong convection to the north of the equator. Also, the strength of ISO convection tends to be weaker during the pIOD years possibly due to the cooler SSTs in the SEIO. Wilson et al. (2013) also documented the reduced (enhanced) strength of low frequency ISO (MJO) related convection over the EEIO during pIOD (nIOD) years, however their study focuses on the time August, September, October, and November. Figure 21 shows the sequence of events we propose to be responsible for weak (strong) northward propagations during pIOD (nIOD) years.

Some studies in the past (e.g., Wang and Xie 1997; Kemball-Cook and Wang 2001; Jiang et al. 2018) observed the strength of the Rossby wave lobe (vortex) in the northern hemisphere to be stronger than the one in the southern hemisphere because of destabilizing caused by the easterly wind shear (Wang and Xie 1997). We see that the strength of the southern hemisphere lobe (Fig. 18a) on day 0 to be slightly stronger than the one in the northern hemisphere mainly because of warmer waters and slightly enhanced specific humidity in SEIO during nIOD years leading to strong Rossby wave response in

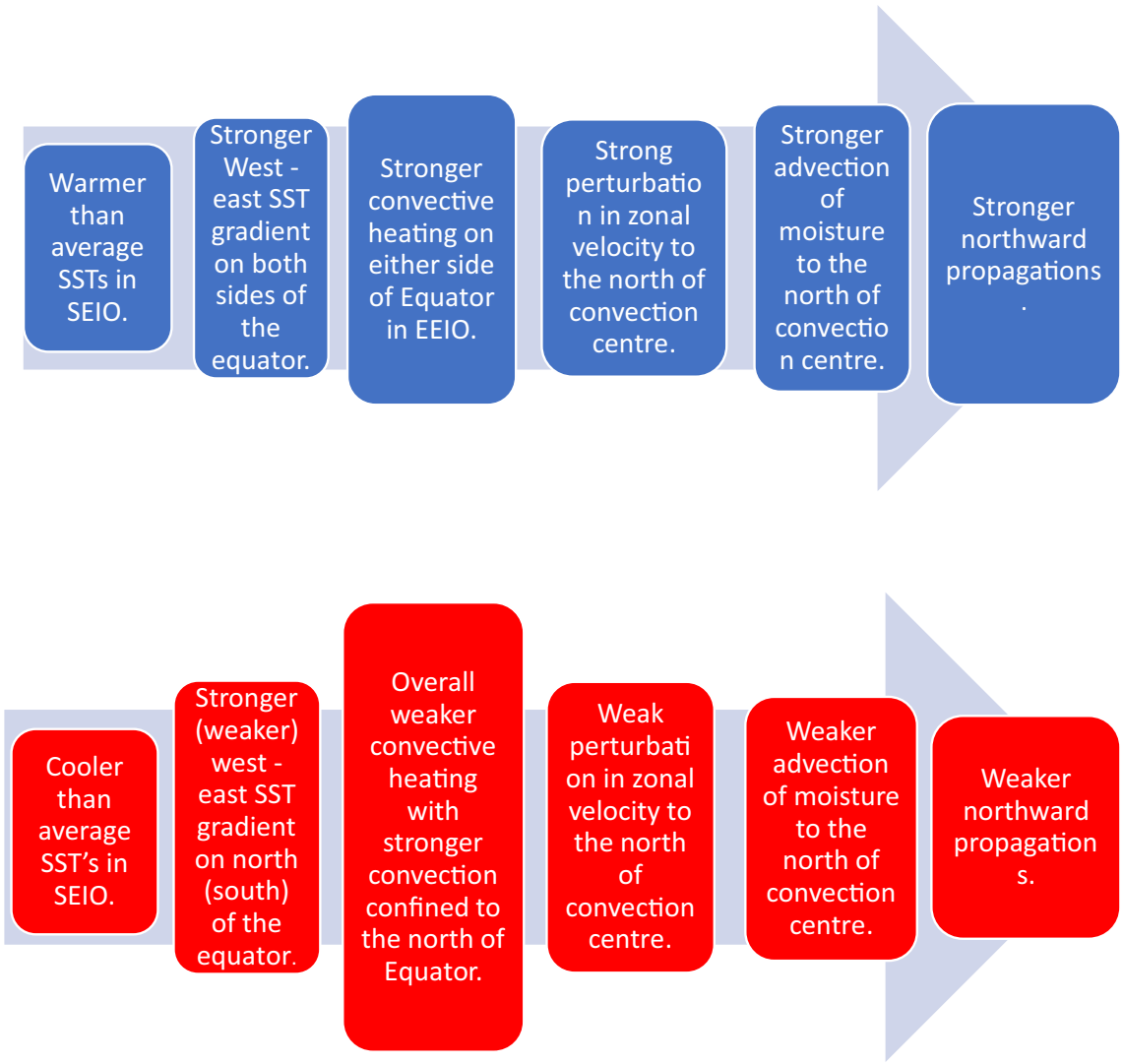

Fig. 21 Sequence of events that are proposed to be responsible for stronger and weaker propagations during nIOD (blue) and pIOD (red) years, respectively

Southern hemisphere. In the following days, the lobe in the northern hemisphere gets stronger, and the one in the southern hemisphere gets weaker (not shown here).

6 Summary and discussion

Northward propagation of intraseasonal oscillations is one of the dominant modes of tropical variability during the monsoon season and are associated with active and break spells of the Indian summer monsoon (Yasunari 1979; Sikka and Gadgil 1980). IOD, an ocean–atmospheric interaction, is considered as an internal mode of variability in the Indian Ocean (Saji et al. 1999). In this study, we address the question: "How do the northward propagations get modulated by IOD?" and "What are the processes responsible for that modulation?" Using NOAA OLR data, we showed that during nIOD years, strong northward propagations of ISO filtered OLR anomalies can be seen from the equatorial region to 20° N (Fig. 4). During pIOD years, the northward propagations are weaker, with the OLR anomalies from the equator barely reaching past 10° N (Fig. 5). Recently, using the moisture mode framework, Jiang et al. (2018) highlighted the role of mean moisture pattern for northward propagation of ISO. Thus, to understand northward propagations weakening during pIOD years, we conducted a moisture entropy budget in this study.

Results suggest that a reduction in the horizontal advection of entropy (moisture) during ISO events is responsible for the weakening of northward propagation. Further analysis revealed that the mean structure of entropy remained

similar across contrasting IOD years, and weaker horizontal advection during pIOD years primarily results from weaker zonal wind perturbations at intraseasonal timescales. During nIOD years, we observed strong zonal wind perturbations to the north of the ISO convection centre (Fig. 17a), but during pIOD years these zonal wind perturbations are weak (Fig. 17b). These weaker zonal wind perturbations result from either change in the structure or strength of convective heating during pIOD years owing to cooler SSTs in SEIO and warmer SSTs in WEIO. At lag 5 days, during nIOD years, the ISO convective heating is symmetric about the equator over the EEIO and adjoining maritime continent. During pIOD years, intense convective heating is mainly confined to the north of the equator and, also the convective heating is strong over WEIO and weak over SEIO. Also, the strength of convection is weaker during the pIOD years. Thus, the equatorial wave dynamics play a crucial role in enhancing (weakening) the northward propagations during nIOD (pIOD) years. To pinpoint the reason for the difference in the Rossby wave response across contrasting IOD years, we plan to perform simple model experiments using Shallow water equations with a prescribed heat source in the future.

The ISMR is influenced by the relative strengths of ElNino/ENSO and IOD (Ashok et al. 2001, 2004). The pIOD event enhances the ISMR in the absence of the ElNino event. However, when they co-occur, the ISMR is dictated by the relative strengths of the IOD and ENSO events (Ashok et al. 2001). For example, 2019 can be considered a year with weak Elnino–strong pIOD and ISMR were 109% of the normal. More interestingly, in June 2019, the rainfall over the Indian subcontinent was 67% of the normal, but the JJAS mean rainfall ended 9% above the normal. This 33% deficit during June 2019 was a response to the SST anomaly outside the Indian ocean (ElNino), while the unusually high September rainfall (152%) was due to the pIOD event (Gadgil et al. 2019; Ratna et al. 2021). Significant anomalies in ISMR are associated with the EQUINOO, and an index that is a linear combination of ENSO and EQUINOO explains the ISMR anomalies in all seasons (Gadgil et al. 2004). The details of the roles of ENSO and EQUINOO in intraseasonal rainfall variations are also documented in Francis and Gadgil (2010).

Nevertheless, "How does the weakening of the northward propagations from the equator result in enhanced ISMR?" needs further studies and investigation. However, it should be noted that the ISMR does not depend only on the northward propagations. Vishnu et al. (2019) observed that the rainfall over the core monsoon zone is attributed to

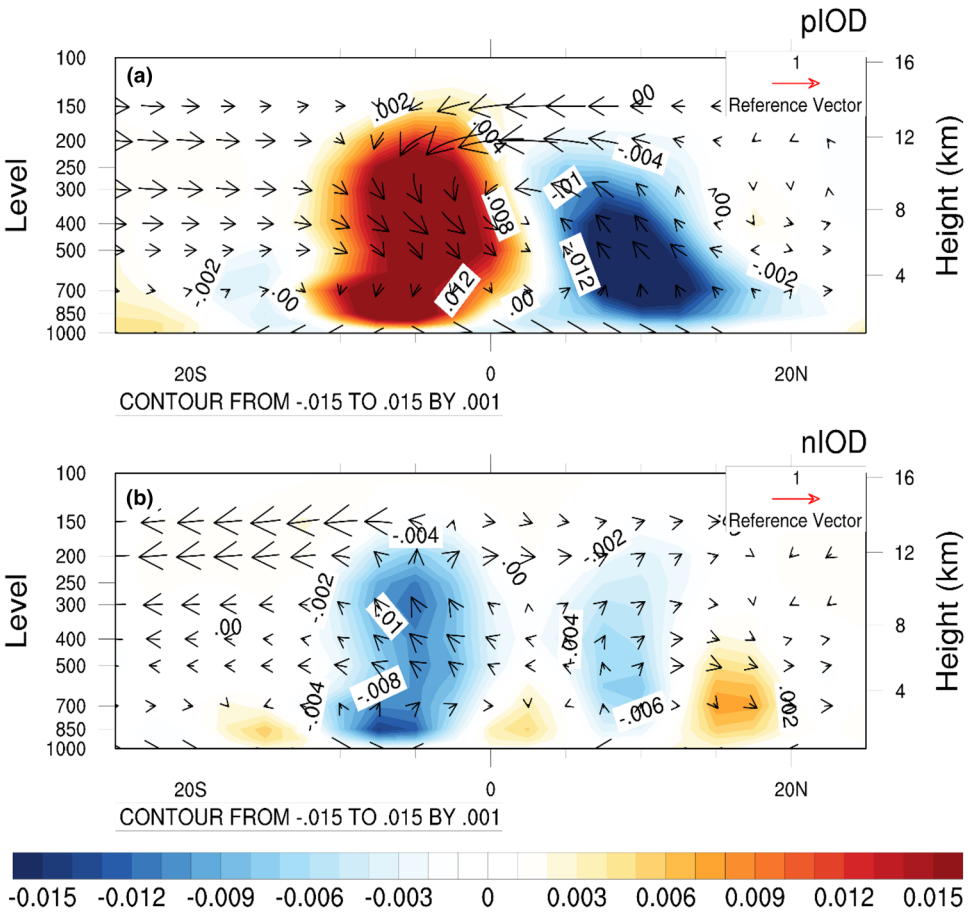

Fig. 22 The JJAS mean anomaly of pressure vertical velocity (pa/s, shaded) and meridional circulation (m/s, vectors), for **a** pIOD and **b** nIOD years. The vertical velocity scale has been enhanced by a factor of 100 (in the vector plot) for easy visualisation. The anomalies are averaged across 70° E–95° E longitudes

the low-pressure systems (LPS) over the Bay of Bengal that move west/northwestward across India. They also observed the track density (which represents the frequency) of the LPS over the head bay is higher during positive EQUINOO years than the negative EQUINOO years. These higher number of LPS enhance the ISMR during positive EQUINOO years. Though we considered the influence of IOD in our work and not the EQUINOO, many of the pIOD years in our work are positive EQUINOO years. Thus, there is a possibility that the frequency of LPS is higher in the pIOD years we have considered but conducting a frequency check is beyond the scope of this work. Nevertheless, in Fig. 22 we show the JJAS anomaly of vertical pressure velocity and the anomalous meridional circulation for pIOD and nIOD years (Table 1). Anomalous ascent can be seen between latitudes 10° N and 15° N over the Indian region during pIOD years (Fig. 22a), and this ascending air crosses the equator and sinks just to the south of the equator. This anomalous ascent over India could be due to an increase in LPS, as pointed out in Vishnu et al. (2019). Also, Vishnu et al. (2019) did not find the differences in the number of northward propagations during different phases of EQUINOO. However, the number of northward propagations in their paper are counted at 90° E. They estimated the events based on a latitude-time plot; instead, we considered the longitudinal band between 70 and 95° E. It can be seen in Fig. 5 that at 90° E during pIOD years, we still see weak northward propagation of OLR anomalies (lag 0 to lead 12). But these propagations are not coherent across the longitudinal band as in nIOD year (Fig. 5). The same incoherent propagations during pIOD years were documented in Ajayamohan et al. (2008).

Supplementary Information The online version contains supplementary material available at https://doi.org/10.1007/s00382-022-06164-w.

Acknowledgements PNV acknowledges partial financial support from J C Bose National Fellowship, SERB, DST, Govt. India, and BoBBLE program funded by Ministry of Earth Sciences, Govt. of India under its Monsoon Mission program. AK acknowledges financial support from MHRD Govt. India, and Grantham fellowship. We thank NOAA for daily gridded OLR data, daily gridded SST data, NCEP for reanalysis data and OAFlux for daily gridded heat flux data. We would like to thank Copernicus Climate Change and Atmospheric Monitoring Services for the radiation data. We also would like to express our sincere gratitude to the anonymous reviewers for sparing their valuable time helping in the betterment and readability of the manuscript.

Funding AK has financial support from MHRD Government of India (GOI) and Grantham fellowship. P.N.V has partial financial support from J C Bose National Fellowship, SERB, DST, Government of India (GOI) and BoBBLE program funded by Ministry of Earth Sciences, Govt. of India under its Monsoon Mission program.

Data availability The data used in this study can be downloaded from https://psl.noaa.gov/data/gridded/data.ncep.reanalysis2.html, https://psl.noaa.gov/data/gridded/data.noaa.oisst.v2.highres.html, http://oaflux.whoi.edu/data.html,https://psl.noaa.gov/data/gridded/data.interp_OLR.html and Hersbach et al. (2018) were downloaded from the Copernicus Climate Change Service (C3S) Climate Data Store.

Code availability All the codes used in this study were written in NCAR Command Language (NCL). Though they are written specifically for this study, they will be provided to anyone on a request to the author through an e-mail.

Declarations

Conflict of interests Authors declare no competing interests.

References

Adames ÁF, Kim D (2016) The MJO as a dispersive, convectively coupled moisture wave: theory and observations. J Atmos Sci 73:913–941. https://doi.org/10.1175/JAS-D-15-0170.1

Adames ÁF, Wallace JM (2015) Three-dimensional structure and evolution of the moisture field in the MJO. J Atmos Sci 72:3733–3754. https://doi.org/10.1175/JAS-D-15-0003.1

Adames ÁF, Wallace JM, Monteiro JM (2016) Seasonality of the structure and propagation characteristics of the MJO. J Atmos Sci 73:3511–3526. https://doi.org/10.1175/JAS-D-15-0232.1

Ajayamohan RS, Rao SA, Yamagata T (2008) Influence of Indian Ocean Dipole on poleward propagation of boreal summer intraseasonal oscillations. J Clim 21:5437–5454. https://doi.org/10.1175/2008JCLI1758.1

Ashok K, Guan Z, Yamagata T (2001) Impact of the Indian Ocean dipole on the relationship between the Indian monsoon rainfall and ENSO. Geophys Res Lett 28:4499–4502. https://doi.org/10.1029/2001GL013294

Ashok K, Guan Z, Saji NH, Yamagata T (2004) Individual and combined influences of the ENSO and Indian Ocean Dipole on the Indian summer monsoon. J Clim 17:3141–3155. https://doi.org/10.1175/1520-0442(2004)017%3c3141:IACIOE%3e2.0.CO;2

Bhat G, Gadgil S, Kumar PVH, Kalsi SR, Madhusoodanan P, Murty VSN, Prasada Rao CVK, Babu VRR (2001) BOBMEX: The Bay of Bengal monsoon experiment. Am Meteorol Soc 82:2217–2243

Bolton D (1980) The computation of equivalent potential temperature. Mon Weather Rev 108:1046–1053

Chen G, Wang B (2021) Diversity of the boreal summer intraseasonal oscillation. J Geophys Res Atmos 126:e2020JD034137. https://doi.org/10.1029/2020JD034137

Francis PA, Gadgil S (2010) Towards understanding the unusual Indian monsoon in 2009. J Earth Syst Sci 119(4):397–415

Fu X, Wang B, Li T, McCreary JP (2003) Coupling between northward-propagating, intraseasonal oscillations and surface temperature in the Indian Ocean. J Atmos Sci 60:1733–1753. https://doi.org/10.1175/1520-0469(2003)060%3c1733:CBNIOA%3e2.0.CO;2

Gadgil S, Srinivasan J (1990) Low frequency variation of tropical convergence zones. Meteorol Atmos Phys 44:119–132

Gadgil S, Srinivasan J, Nanjundiah RS, Kumar KK, Munot AA, Kumar KR (2002) On forecasting the Indian summer monsoon: the intriguing season of 2002. Curr Sci 4:394–403

Gadgil S, Vinayachandran PN, Francis PA, Gadgil S (2004) Extremes of the Indian summer monsoon rainfall, ENSO, and equatorial Indian Ocean oscillation. Geophys Res Lett 31:L12213. https://doi.org/10.1029/2004GL019733

Gadgil S, Francis PA, Vinayachandran PN (2019) Summer monsoon of 2019: understanding the performance so far and speculating about the rest of the season. Curr Sci 117(5):783

Gill AE (1980) Some simple solutions for heat-induced tropical circulation. Q J R Meteorol Soc 106:447–462

Goswami BN, Sengupta D, Kumar GS (1998) Intraseasonal oscillations and interannual variability of surface winds over the Indian monsoon region. J Earth Syst Sci 107:45–64. https://doi.org/10.1007/BF02842260

Hersbach H, Bell B, Berrisford P, Biavati G, Horányi A, Muñoz Sabater J, Nicolas J, Peubey C, Radu R, Rozum I, Schepers D, Simmons A, Soci C, Dee D, Thépaut J-N (2018) ERA5 hourly data on single levels from 1979 to present. Copernicus Climate Change Service (C3S) Climate Data Store (CDS). https://doi.org/10.24381/cds.adbb2d47

Huang B, Liu C, Banzon VF, Freeman E, Graham G, Hankins B, Smith TM, Zhang H-M (2020) NOAA 0.25-degree daily optimum interpolation sea surface temperature (OISST), Version 2.1 [SST anomaly]. NOAA National Center for Environmental Information

Jiang X (2017) Key processes for the eastward propagation of the Madden–Julian Oscillation based on multimodel simulations. J Geophys Res Atmos 122:755–770. https://doi.org/10.1002/2016JD025955

Jiang X, Li T, Wang B (2004) Structures and mechanisms of the northward propagating boreal summer intraseasonal oscillation. J Clim 17:1022–1039. https://doi.org/10.1175/1520-0442(2004)017%3c1022:SAMOTN%3e2.0.CO;2

Jiang X, Adames AF, Zhao M, Waliser D, Maloney E (2018) A unified moisture mode framework for Figonality of the Madden Julian oscillation. J Clim 31(11):4215–4224. https://doi.org/10.1175/JCLI-D-17-0671.1

Karmakar N, Chakraborty A, Nanjundiah RS (2017) Space-time evolution of the low- and high-frequency intraseasonal modes of the Indian Summer Monsoon. Mon Weather Rev 145(2):413–435. https://doi.org/10.1175/MWR-D-16-0075.1

Kemball-Cook S, Wang B (2001) Equatorial waves and air–sea interaction in the boreal summer intraseasonal oscillation. J Clim 14:2923–2942. https://doi.org/10.1175/1520-0442(2001)014%3c2923:EWAASI%3e2.0.CO;2

Kiranmayi L, Maloney ED (2011) Intraseasonal moist static energy budget in reanalysis data. J Geophys Res 116:D21117. https://doi.org/10.1029/2011JD016031

Krishnamurti T, Subramanyam D (1982) The 30–50 days mode at 850 mb during MONEX. J Atmos Sci 39:2088–2095

Krishnamurti TN, Osterhof DK, Mehta AV (1988) Air–sea interaction on the time scale of 30–50 days. J Atmos Sci 45:1304–1322. https://doi.org/10.1175/1520-0469(1988)045,1304:AIOTTS.2.0.CO;2

Lawrence DM, Webster PJ (2002) The boreal summer intraseasonal oscillation: relationship between northward and eastward movement of convection. J Atmos Sci 59:1593–1606. https://doi.org/10.1175/1520-0469(2002)059%3c1593:TBSIOR%3e2.0.CO;2

Liebmann B, Smith CA (1996) Description of a complete (interpolated) outgoing longwave radiation dataset. Bull Am Meteorol Soc 77:1275–1277

Lindzen RS, Nigam S (1987) On the role of sea surface temperature gradients in forcing low-level winds and convergence in the tropics. J Atmos Sci 44:2418–2436

Maloney ED (2009) The moist static energy budget of a composite tropical intraseasonal oscillation in a climate model. J Clim 22:711–729. https://doi.org/10.1175/2008JCLI2542.1

Misra V, Pantina P, Chan SC, DiNapoli S (2012) A comparative study of the Indian summer monsoon hydroclimate and its variations in three reanalyses. Clim Dyn 39:1149–1168. https://doi.org/10.1007/s00382-012-1319-y

Misra V, Mishra A, Bhardwaj A (2018) Simulation of the intraseasonal variations of the Indian Summer Monsoon in a Regional Coupled Ocean-Atmosphere Model. J Clim. https://doi.org/10.1175/JCLI-D-17-0434.1

Nanjundiah RS, Srinavasan J, Gadgil S (1992) Intraseasonal variation of the Indian summer monsoon. II. Theoretical aspects. J Meteorol Soc Jpn 70:529–549

Ratna SB, Cherchi A, Osborn TJ, Joshi M, Uppara U (2021) The extreme positive Indian Ocean Dipole of 2019 and associated Indian Summer Monsoon. Geophys Res Lett. https://doi.org/10.1029/2020GL091497

Raymond DJ, Fuchs Z (2009) Moisture modes and the Madden–Julian Oscillation. J Clim 22:3031–3046. https://doi.org/10.1175/2008JCLI2739.1

Saji NH, Yamagata T (2003) Possible impacts of Indian Ocean Dipole mode events on global climate. Clim Res 25:151–169

Saji NH, Goswami BN, Vinayachandran PN, Yamagata T (1999) A dipole mode in the tropical Indian ocean. Nature 401:360–363. https://doi.org/10.1038/43854

Sengupta D, Ravichandran M (2001) Oscillations of Bay of Bengal sea surface temperature during the 1998 summer monsoon. Geophys Res Lett 28:2033–2036

Sengupta D, Goswami BN, Senan B (2001) Coherent intraseasonal oscillations of ocean and atmosphere during the Asian summer monsoon. Geophys Res Lett 28:4127–4130

Sikka DR, Gadgil S (1980) On the maximum cloud zone and the ITCZ over Indian longitudes during the southwest monsoon. Mon Weather Rev 108:1840–1853

Sobel A, Maloney E (2012) An idealized semi-empirical framework for modeling the Madden–Julian Oscillation. J Atmos Sci 69:1691–1705. https://doi.org/10.1175/JAS-D11-0118.1

Sobel A, Maloney E (2013) Moisture modes and the eastward propagation of the MJO. J Atmos Sci 70:187–192

Vinayachandran PN, Francis PA, Rao SA (2009) Indian Ocean Dipole-processes and impacts. In: Mukunda N (ed) Current trends in Science. Indian Academy of Science, Bangalore

Vishnu S, Francis PA, Ramakrishna SSVS et al (2019) On the relationship between the Indian summer monsoon rainfall and the EQUINOO in the CFSv2. Clim Dyn 52:1263–1281. https://doi.org/10.1007/s00382-018-4190-7

Wang B, Xie X (1997) A model for the boreal summer intra-seasonal oscillation. J Atmos Sci 54:72–86

Webster PJ (1983) Mechanisms of low-frequency variability: surface hydrological effects. J Atmos Sci 40:2110–2124

Webster PJ, Moore A, Loschnigg J, Leban M (1999) Coupled ocean-atmosphere dynamics in the Indian Ocean during 1997–98. Nature 401:356–360

Wilson EA, Gordon AL, Kim D (2013) Observations of the Madden Julian Oscillation during Indian Ocean Dipole events. J Geophys Res Atmos. https://doi.org/10.1002/jgrd.50241

Yasunari T (1979) Cloudiness fluctuations associated with the Northern Hemisphere Summer Monsoon. J Meteorol Soc Jpn 57:227–242

Yu L, Jin X, Weller RA (2008) Multidecade global flux datasets from the objectively analyzed air–sea fluxes (OAFlux) project: latent and sensible heat fluxes, ocean evaporation, and related surface meteorological variables. Woods Hole Oceanographic Institution, Woods Hole, OAFlux Project Tech. Rep. OA-2008-01